

Department of Physics and Astronomy
University of Heidelberg

Bachelor Thesis in Physics
submitted by

Anton Eberhardt

born in Heidenheim an der Brenz (Germany)

November 2020

Strategy for measuring the mass of ${}^3_{\Lambda}H$ with the ALICE detector

This Bachelor Thesis has been carried out by Anton Eberhardt at the
Physikalisches Institut of the University of Heidelberg
under the supervision of
Prof. Dr. Silvia Masciocchi

Abstract

The high center-of-mass energies in heavy-ion collisions at the LHC enable the production of a state of matter called the Quark Gluon Plasma (QGP). During these collisions a large number of particles is produced. In particular, the production of hypernuclei, like for example the hypertriton (${}^3_{\Lambda}H$), has been observed. It is currently not clear how ${}^3_{\Lambda}H$ can form in a system characterized by temperatures much higher than its binding energy. Its short lifetime is also not yet fully explained, which is an open question known as the ${}^3_{\Lambda}H$ -lifetime puzzle. Since the precise determination of the separation energy B_{Λ} of the Λ to the deuteron could be crucial in solving the lifetime puzzle, this thesis focuses on devising a strategy for measuring the mass of ${}^3_{\Lambda}H$ (and with that the separation energy B_{Λ}) via its 3-body decay channel, using data from Pb-Pb collisions at $\sqrt{s_{NN}}=5.02$ TeV gathered with the ALICE detector at the LHC. For this, a Monte Carlo (MC) simulation will be studied to compare different models for fitting the measured mass peaks. Various effects causing the obtained mass values to differ from the simulated ones will be investigated. At the end, a possible candidate selection for the analysis of real data will be applied and its performance will be discussed.

Zusammenfassung

Die hohen Schwerpunktsenergien in Schwerionenkollisionen am LHC ermöglichen die Produktion eines Zustandes der Materie, der Quark Gluon Plasma (QGP) genannt wird. Eine Vielzahl an Teilchen wird während solchen Kollisionen produziert, insbesondere wurde auch die Produktion von Hypernuklei, wie zum Beispiel dem Hypertriton (${}^3_{\Lambda}H$), beobachtet. Es ist momentan nicht bekannt, wie ${}^3_{\Lambda}H$ in einem System entstehen kann, das durch Temperaturen charakterisiert ist, die seine Bindungsenergie stark überschreiten. Auch die kurze Lebenszeit kann bis jetzt noch nicht komplett erklärt werden, was als das ${}^3_{\Lambda}H$ -Lifetime Puzzle bekannt ist. Da die genaue Bestimmung der Separationsenergie B_{Λ} des Λ zum Deuteron ausschlaggebend für die Lösung des Lifetime Puzzles sein könnte, beschäftigt sich diese Arbeit mit der Bestimmung einer Strategie für die Messung der ${}^3_{\Lambda}H$ -Masse (und damit der Messung der Separationsenergie B_{Λ}) über seinen 3-Körper Zerfall mithilfe der Daten von Pb-Pb Kollisionen bei $\sqrt{s_{NN}}=5.02$ TeV, aufgenommen mit dem ALICE Detektor am LHC. Dafür wird eine Monte Carlo (MC) Simulation untersucht, um verschiedene Modelle zum Fitten von den erhaltenen Massenverteilungen zu vergleichen. Einige Effekte, die einen Unterschied zwischen gemessenen und simulierten Werten für die Masse zur Folge haben, werden betrachtet. Zum Schluss wird eine mögliche Kandidatenselektion für die Analyse des echten Datensets angewendet und ihre Wirksamkeit wird diskutiert.

Contents

1	Introduction	1
1.1	Confinement and asymptotic freedom	2
1.2	Heavy-ion collisions and the QGP	4
1.3	The hypertriton (${}^3_{\Lambda}H$)	5
1.3.1	Lifetime puzzle	5
1.3.2	Decay channels	7
2	ALICE	9
2.1	The coordinate system	10
2.2	Subdetectors	12
2.2.1	The Inner Tracking System (ITS)	12
2.2.2	The Time-Projection-Chamber (TPC)	12
2.2.3	The Time-Of-Flight (TOF) detector	13
2.3	Tracking and reconstruction	13
3	Analysis tools	15
3.1	The KFparticle vertexing package	15
3.2	Monte Carlo Sample	16
3.2.1	Preselections for the MC dataset	18
4	Analysis and Results	21
4.1	Expected yield of ${}^3_{\Lambda}H$ in three-body decay	21
4.2	Determination of the model used to fit the mass distributions	23
4.3	Systematic mass shift introduced by the KF particle package	30
4.4	Wrongly assigned hits in the ITS	34
4.5	Selection of ${}^3_{\Lambda}H$ -candidates	40
4.5.1	Event selection	40
4.5.2	Candidate selection	40
4.5.3	Signal in data collected by ALICE	42
4.5.4	Mass resolution in Monte Carlo simulations	45
5	Conclusion and Outlook	47

Chapter 1

Introduction

All visible matter inside the observable universe is assumed to consist of the same fundamental building blocks, summarized in the standard model of particle physics (SM) (see Fig. 1.1). It consists of twelve *fermions* and four types of *gauge bosons*, which mediate the fundamental forces: The strong force, which is mediated by the *gluons*, the weak force, mediated by the *Z-boson* and the two charged *W[±]-bosons* and the electromagnetic force, which is mediated by *photons*¹.

The twelve *fermions* (and their antimatter counterparts, which have the exact same mass but the opposite charge) can be further categorized as quarks and leptons in three so called *generations of matter*.

There are three charged leptons, which experience the electromagnetic and the weak force and three uncharged leptons, called *neutrinos*, which experience only the weak force. While leptons can exist in unbound states, quarks, which experience all fundamental forces, are only observed in bound states, due to an effect called *confinement*, which is a result of the nature of the strong force, which is accurately described by *quantum chromodynamics* (QCD, see e.g. [21]). There are two types of these bound states which are regularly observed in experiments: the *mesons*, which are composed of one quark and one antiquark and the *baryons* (*antibaryons*), which are composed of three quarks (antiquarks). Most of the visible matter is made up of particles of the first generation, however it is hypothesized that stable matter consisting of heavier particles can exist in extreme environments, for example inside neutron stars.

To investigate the nature of these heavier particles, particle accelerators were built and currently, the most powerful one is the *Large Hadron Collider* (LHC) at CERN (which stands for "Conseil Européen pour la Recherche Nucléaire") in Geneva. At such facilities, different particles are accelerated to high energies and brought to collision, creating extreme conditions from which one can gather the data crucial for explaining some fundamental problems in physics. The ALICE experiment is a particle detector at one of the collision points of the LHC.

In this thesis, data from highly relativistic heavy-ion (lead-lead) collisions, taken with ALICE, will be used to investigate properties of the lightest known *hypernucleus* (a nucleus which includes a baryon containing a quark of the second generation): the Hypertriton (${}^3_{\Lambda}H$) consists of one proton (uud²), one neutron (udd) and one Λ -baryon (uds). The goal is to analyze if data from ALICE can be used to accurately

¹Gravity is also considered a fundamental force, but it has not yet been included in the SM successfully

²this describes the valence quark content, compare to Fig. 1.1

measure the mass of such particles, which will be done by studying a Monte Carlo (MC) simulated dataset. Also, it will be attempted to measure the mass of this hypernucleus and to use this measurement to calculate the separation energy of the Λ to the deuteron core. The three baryons of the ${}^3_\Lambda H$ are bound due to the strong force, however, the mechanism responsible for this is not yet well understood and can't be calculated from first principles of QCD, which is why current explanations only consist of effective models like in [3]. Explaining the effective interaction between hadrons with different quark contents is one of the big challenges in modern nuclear physics. The lifetime of ${}^3_\Lambda H$, which is measured to be significantly lower than the lifetime of a free Λ^3 , indicates that measuring the properties of ${}^3_\Lambda H$ will help advancing in this field of study.

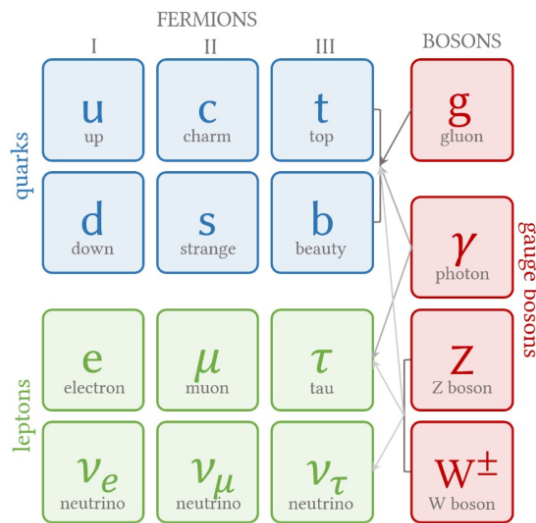


Figure 1.1: Particles in the standard model for particle physics (illustration from [20])

1.1 Confinement and asymptotic freedom

The aforementioned confinement of quarks arises from the fact that the gluons themselves carry *color charge*, which is a property of particles that allows them to feel the strong nuclear force. Two particles with color charge interact with each other by exchanging gluons and since they also carry a color charge, they interact with other gluons that are being exchanged. This gluon-gluon self-interaction results in a constant energy density between the two initial particles, meaning that the energy stored in the color field between them is proportional to the distance from each other. With this in mind, it should be clear that separating two color charged quarks takes an infinite amount of energy, which is why all quarks arrange themselves in *colorless* states like baryons and mesons.

However, the coupling constant α_s of the strong force depends on the transferred

³this will be explained in more detail in section 1.3.1

momentum q^2 :

$$\alpha_s(q^2) = \frac{\alpha_0}{1 + B\alpha_0 \cdot \ln\left(\frac{q^2}{\mu^2}\right)} \quad (1.1)$$

Here, α_0 is some known value of α_s and μ is a constant, which depends on the choice of α_0 . B is given by

$$B = \frac{11N_c - 2N_f}{12\pi}$$

where N_c is the number of different color charges and N_f is the number of quark flavors.

This effect is called the *running* of the coupling constant and was experimentally confirmed in several different measurements (see figure 1.2 from [21], page 259). It gives rise to the possibility of quarks existing in quasi-free states inside high temperature and high pressure regions (since q^2 increases with temperature and pressure). The existence of this *asymptotic freedom* suggests that at high energy densities phase transitions between hadronized (confined) matter and unconfined matter, called the *quark-gluon plasma* (QGP), can occur. As will be explained in the next section, the extreme conditions achieved during ultra-relativistic heavy-ion collisions are able to produce small amounts of QGP, making it able to investigate its physical properties and its transition back to confined matter (*hadronisation*).

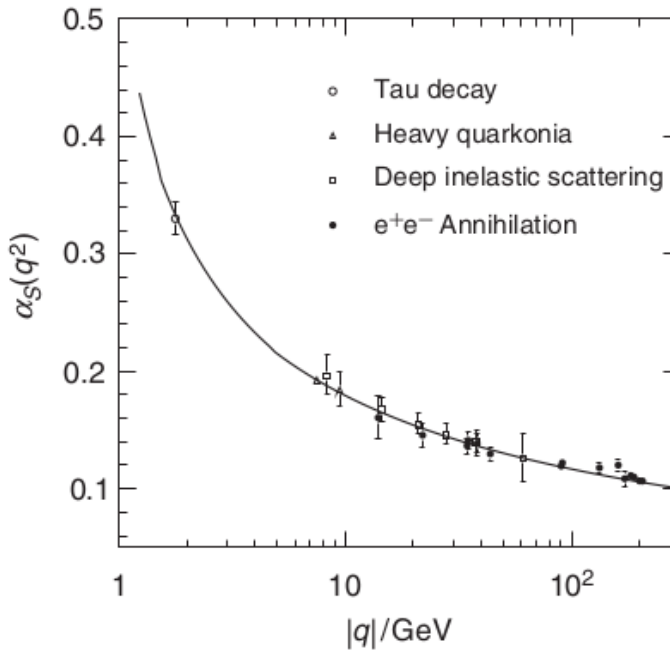


Figure 1.2: Experimental evidence on the running of the strong coupling constant α_s (taken from [21], page 259)

1.2 Heavy-ion collisions and the QGP

In modern particle accelerators heavy ions like lead and gold nuclei can be accelerated to energies high enough that during a collision of two such nuclei they do not interact with each other as a whole, but rather their constituents interact with each other separately. The nuclei and even their contained nucleons interpenetrate each other, while the quarks inside them constantly interact with each other. At this point, the system is in a state of very high temperature and very high energy density, which is comparable to the state of the early universe a few microseconds after the big bang, where all existing matter is assumed to have existed as the previously mentioned QGP [17]. The system expands and cools down, causing particles with colour charge to hadronize again. In the QCD phase diagram the early universe and, since they are very similar, also the QGP after a heavy-ion collision follow the path indicated by the dark green line in figure 1.3a. The plot also indicates that there is no first order phase transition between QGP and hadronized matter at low baryon chemical potentials μ_B . Instead of a sharp phase transition the medium undergoes a rapid crossover at a critical temperature T_c as can also be seen in figure 1.3b. Theoretical models predict a *critical point* at higher μ_B , where the crossover becomes a first order phase transition [4].

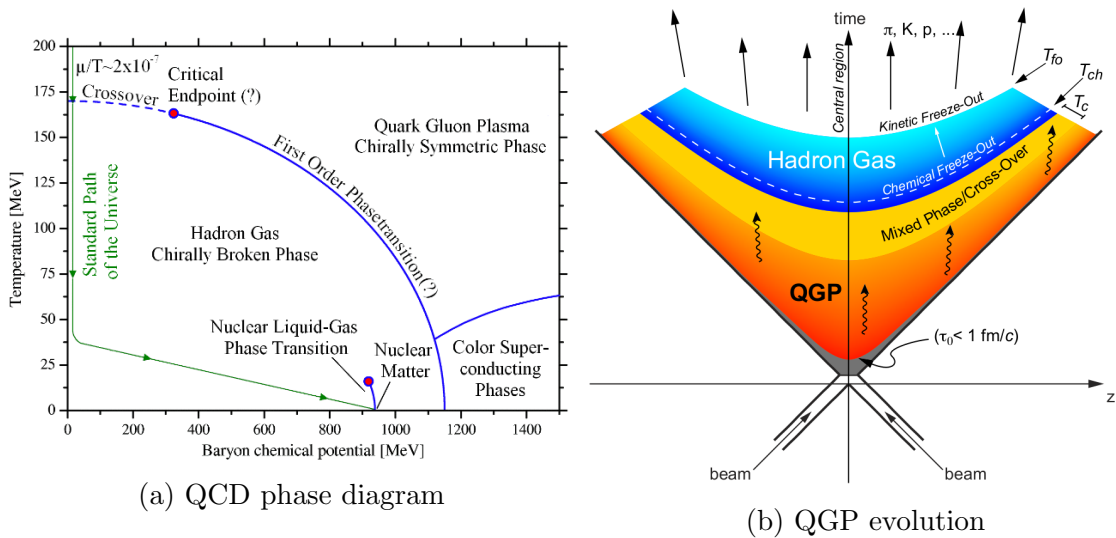


Figure 1.3: (a) QCD phase diagram with the path of the early universe/the QGP in heavy-ion collisions (taken from [4]), (b) space-time evolution of the system after a heavy-ion collision (taken from [22], page 10)

In the case of a heavy-ion collision at the LHC, the energy density in the collision is high enough (above $1 \text{ GeV}/\text{fm}^3$) that the formation of QGP is expected. The evolution of such system is expected to look roughly like 1.3b: two Lorentz contracted nuclei collide at $t = 0$ and $z = 0$ and their constituent partons interact with each other until a small amount of QGP in thermal equilibrium is formed. This QGP-droplet expands and cools until it reaches the temperature $T_c \approx 200 \text{ MeV}$ [17], where the crossover into hadronized matter begins. After the *chemical freeze-out* at the temperature $T_{ch} \approx T_c$ all of the QGP is hadronized and the resulting particles have stopped to interact inelastically, thus the abundances of particles are fixed. However,

the particles still undergo elastic scattering inside the newly formed hadron gas until the system has expanded and cooled off sufficiently. After the temperature drops below $T_{fo} \approx 130$ MeV [17], the elastic scatterings stop (*kinetic freeze-out*), fixing all particle momenta.

By measuring the abundances of the different particle species as well as their properties, one can gather the experimental data needed to compare different theoretical models describing the hadronisation process. This data can also be used to improve the current understanding of not well known particle interactions like for example the interaction between hyperons and nucleons (YN-interactions), which is one of the goals in the study of hypernuclei. The nature of these interactions could also explain some astronomical phenomena like the existence of neutron stars above a certain mass (around two times the mass of the sun), which were observed and measured accurately, but cannot be explained with the current models for the very dense type of matter expected to exist inside neutron stars ([5]).

1.3 The hypertriton (${}^3_{\Lambda}H$)

1.3.1 Lifetime puzzle

As already mentioned, the *Hypertriton* (${}^3_{\Lambda}H$) is the lightest known hypernucleus. The separation energy of the lambda to the deuteron core is only around $B_{\Lambda} = 130$ keV [9], which gives ${}^3_{\Lambda}H$ a so called halo structure, as the small separation energy results in a *Root Mean Square* (RMS) radius⁴ of roughly 10.6 fm [6]. From a theoretical standpoint, this should indicate that the interaction between the Λ and the deuteron core is rather weak and the lifetime of ${}^3_{\Lambda}H$ should be close to that of a free Λ . However, experimental evidence of the recent years indicate that the lifetime is in fact measured to be systematically lower, as can be seen in figure 1.4. A weighted average of all measurements results in a lifetime of $\tau = 206^{+15}_{-13}$ ps (orange band in figure 1.4), whereas the reported lifetime of a free Λ is $\tau_{\Lambda} = (263.2 \pm 2.0)$ ps (black line). Even though the ${}^3_{\Lambda}H$ -lifetime measurements still have large statistical and systematic uncertainties, the current world average deviates from the lifetime of a free Λ by more than 3σ . These uncertainties are expected to reduce with the large amount of data that will be gathered in Run 3 and 4 of the LHC. A measurement of the separation energy B_{Λ} could be helpful in comparing the wide range of different theoretical predictions (colored dashed lines), since a high separation energy would imply a stronger interaction between the Λ and the deuteron, which is expected to lead to a shorter ${}^3_{\Lambda}H$ -lifetime.

⁴this can be interpreted as the average distance of the Λ -particle to the deuteron core

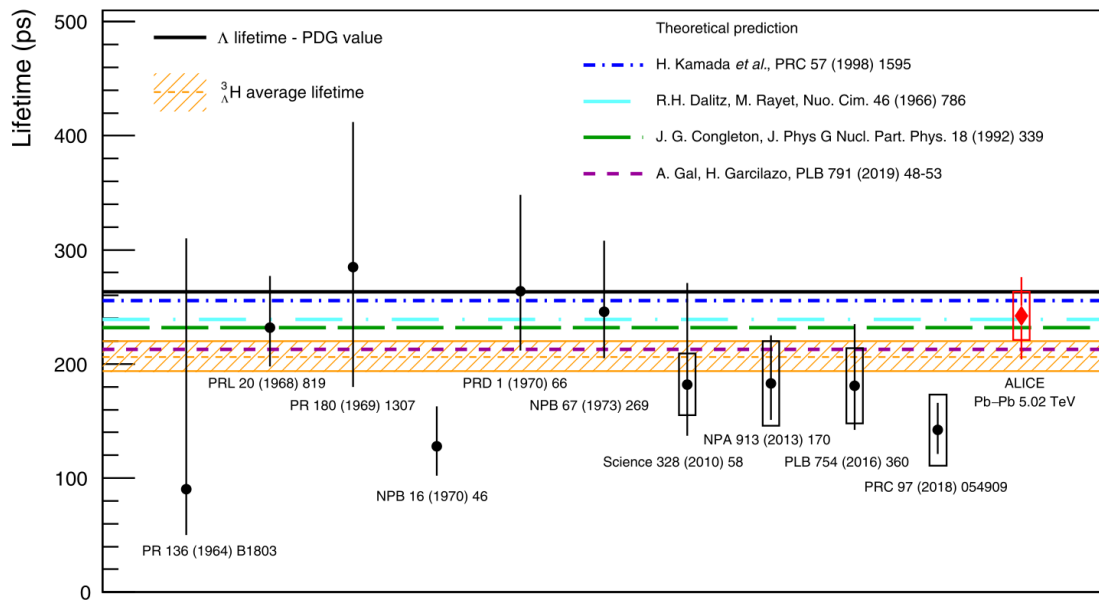


Figure 1.4: All measurements of the ${}^3_{\Lambda}H$ compared to various theoretical predictions. The boxes around the data points represent the systematic uncertainties and the line the statistical uncertainties. (Figure taken from [6])

1.3.2 Decay channels

${}^3_{\Lambda}H$ decays preferably via mesonic decay channels involving protons (p), neutrons (n) and pions (π), as well as heavier particles like deuterons (d), tritons (3H) and helium-3 cores (${}^3\text{He}$). These decay channels are, ordered from highest to lowest *Branching Ratio* (BR): ${}^3_{\Lambda}H \rightarrow d + p(n) + \pi^{-}(\pi^0)$, ${}^3_{\Lambda}H \rightarrow {}^3\text{He}({}^3H) + \pi^{-}(\pi^0)$ and ${}^3_{\Lambda}H \rightarrow p + p(n) + n + \pi^{-}(\pi^0)$. Since most detector systems in ALICE are designed to measure charged particles (see section 2.2), the decay channels involving neutral particles like neutrons and π^0 will not be considered for most analyses. While there are also two nonmesonic decay channels (${}^3_{\Lambda}H \rightarrow d + n$ and ${}^3_{\Lambda}H \rightarrow p + n + n$), they only amount for a small portion of decays [14] and they also involve neutrons. Therefore, the two most promising decay channels for this type of investigation are

$${}^3_{\Lambda}H \rightarrow d + p + \pi^{-} \quad (1.2)$$

and

$${}^3_{\Lambda}H \rightarrow {}^3\text{He} + \pi^{-} . \quad (1.3)$$

which have a BR of roughly 40% and 25% respectively [22]. In this thesis, the focus will lie on the three-body decay (equation 1.2), which has a higher branching ratio, but is expected to have a significantly smaller reconstruction efficiency than the two-body decay: the number of reconstructed ${}^3_{\Lambda}H$ is reduced due to the limited acceptance of detectors, which, in this case, is applied to three instead of two particles. Additionally, the *combinatorial background* is significantly larger for this decay channel, since a heavy-ion collision produces about 300 times more deuterons than ${}^3\text{He}$ -cores and about 300 times more protons than deuterons [8]. This, and the fact that one needs to recombine 3 instead of 2 particles for the reconstruction, increases the amount of candidates that were reconstructed from particles produced in the primary collision. To compensate this effect one needs to apply stricter selection criteria, which will inevitably lead to decreased efficiency.

Chapter 2

ALICE

The *Large Hadron Collider* (LHC) is the largest segment of the accelerator complex at CERN in Geneva and is currently the most powerful particle accelerator in the world (in terms of center-of-mass energy and luminosity). It accelerates protons and/or heavy ions (mostly lead ions) to almost the speed of light and induces collisions between them. The center of mass energy of the colliding particles can reach up to 13 TeV for pp collisions and up to 5.02 TeV per nucleon pair for Pb-Pb collisions. ALICE, which stands for *A Large Ion Collider Experiment*, is a particle detector at one of the eight collision points of the LHC. It was designed to investigate collisions of heavy ions and the formation of QGP within them, but it also takes data from pp- and Pb-p-collisions.

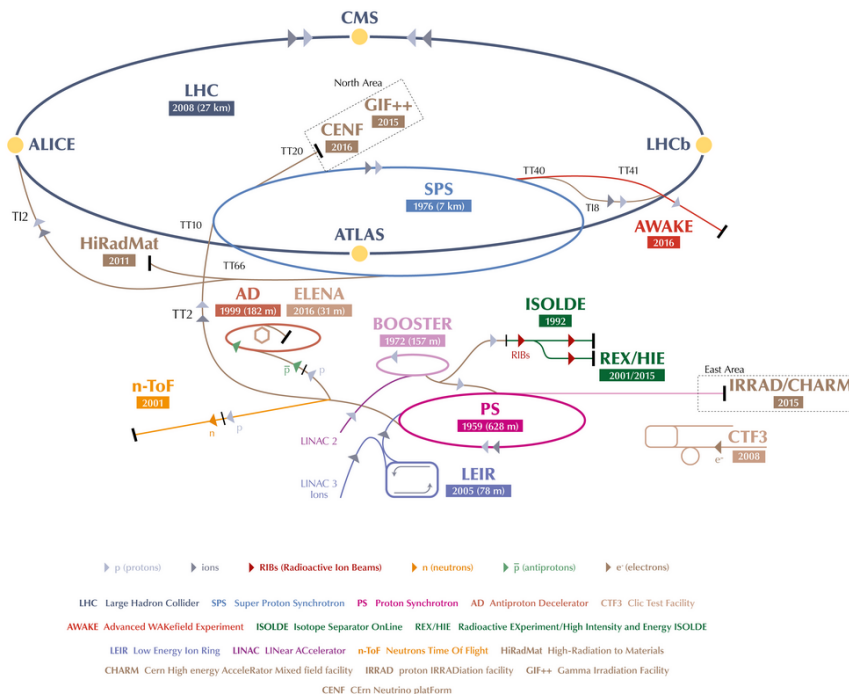


Figure 2.1: The accelerator complex at CERN, the collision points are depicted as large yellow dots on the LHC ring [13].

ALICE is a complex apparatus consisting of 18 detector systems working together and optimized to investigate QCD matter created during ultrarelativistic heavy-ion collisions [22]. Compared to pp-collisions, heavy-ion collisions produce much larger *charged particle multiplicity densities*, which makes it harder to distinguish single tracks from each other, especially in regions close to the collision point. The detector systems of ALICE were designed to have excellent particle identification (PID) capabilities in a large range of momentum at such extreme multiplicities, enabling unprecedented possibilities in the study of strongly interacting matter. In the following sections, the basic functionalities of ALICE will be discussed and an overview of the most important subdetectors will be given. A complete description of ALICE can be found in [15]¹ and [12].

2.1 The coordinate system

ALICE uses a coordinate system aligned with the geometry of the experiment. It is a right-handed orthogonal Cartesian system with the beam pipe being parallel to the z axis and the x axis pointing towards the center of the LHC accelerator ring. The definitions of the azimuthal angle ϕ and the polar angle θ are illustrated in figure 2.2, which also shows the directions of the axes.

In heavy-ion collisions, the colliding particles and their constituents often won't be stopped completely ($p_z = 0$) during the collision, which is why most resulting particles are boosted along the z -axis. To describe detector acceptances independent from this effect, it is useful to define Lorentz-invariant variables like the *rapidity* y

$$y = \frac{1}{2} \ln \frac{E + p_z c}{E - p_z c} \quad (2.1)$$

which, for high momentum particles ($E \gg mc^2$), is equal to the *pseudorapidity* η

$$\eta = \frac{1}{2} \ln \frac{|p| + p_z}{|p| - p_z} = -\ln \left[\tan \left(\frac{\theta}{2} \right) \right] \quad (2.2)$$

which only depends on the polar angle θ . Therefore, the pseudorapidity is often used to describe the range of acceptance for the different detector systems. An illustration of the full ALICE apparatus can be seen in figure 2.3 with a zoom on the detectors closest to the beam pipe. The systems utilized in this investigation are all located in the *central barrel*, one of the three main parts of ALICE. For this thesis, the most important ones are the *Inner Tracking System* (ITS) and the *Time Projection Chamber* (TPC), which have an acceptance of $|\eta| < 0.9$ (except for the inner layer of the ITS, which has an acceptance of up to $|\eta| < 1.98$), as well as full azimuthal coverage. All detectors in the central barrel are embedded in a solenoid providing a magnetic field of $B = 0.5$ T. The other two main parts of ALICE are the *MUON Spectrometer* and the *Forward Multiplicity Detectors*, a detailed description of which can also be found in [15].

¹The information presented in this chapter was taken from here unless otherwise specified

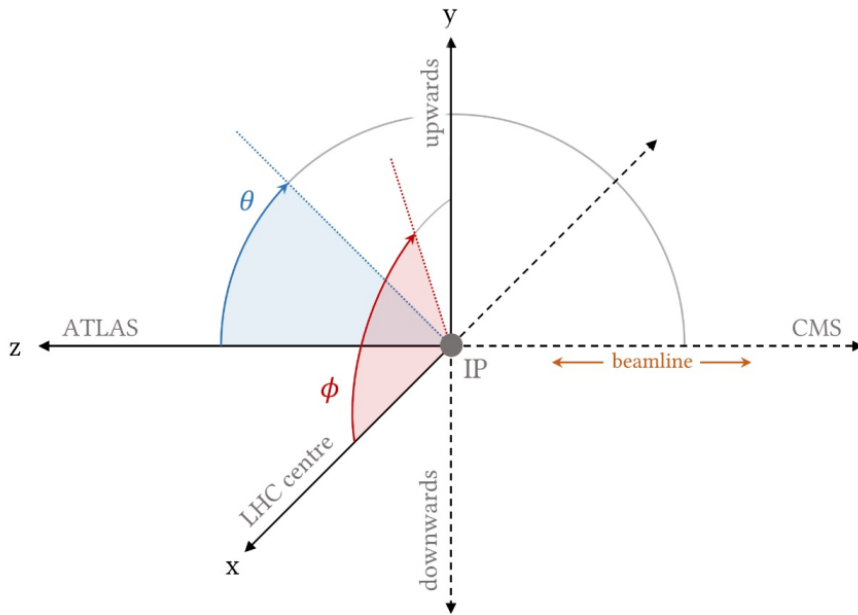


Figure 2.2: Coordinate system used in ALICE (taken from [20])

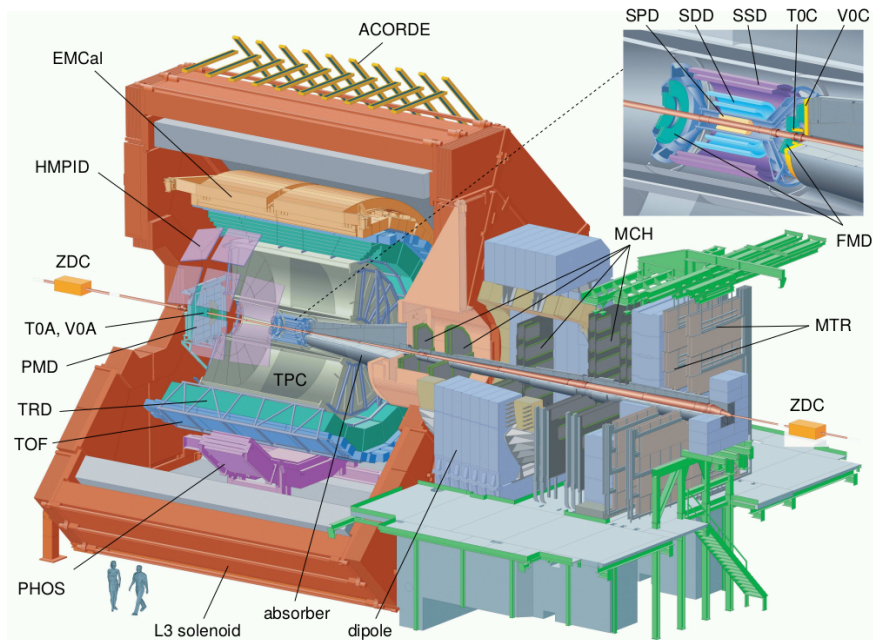


Figure 2.3: Detailed illustration of the ALICE experiment at CERN LHC, the detector systems closest to the beam pipe have been enlarged.

2.2 Subdetectors

2.2.1 The Inner Tracking System (ITS)

The ITS is the detector system closest to the beam pipe and it consists of 6 cylindrical layers of silicon detectors (see figure 2.3): the two inner layers are *Silicon Pixel Detectors* (SPD), where the first layer was constructed to be as close to the beam pipe as possible. The next two layers are *Silicon Drift Detectors* (SDD) and finally, the last two layers are *Silicon Strip Detectors* (SSD), where the radius of the last layer was chosen to optimize the matching of tracks in the ITS with signals in the TPC. The main task of the ITS is the determination of the position of the primary vertex as well as the measurement of the *impact parameter*² of secondary tracks from weak decays of particles containing heavy-flavor quarks like charm and beauty. For this, the SPD layers were designed to have a very high spatial resolution, as they operate in regions, where a track density of up to 50 cm^{-2} is expected during heavy ion collisions. This enables the reconstruction of primary vertices and impact parameters with a resolution of up to $60 \text{ }\mu\text{m}$ in the azimuthal plane. Additionally to a 2D spatial measurement, the four outer layers of the ITS are able to measure the specific ionization energy loss dE/dx of the tracks traversing, enabling PID of low momentum particles.

2.2.2 The Time-Projection-Chamber (TPC)

The TPC surrounds the ITS and is the main tracking detector of the central barrel. It is used to determine momenta of charged particles and to identify them. The TPC covers a very large transverse momentum range from about 0.1 GeV to 100 GeV while still maintaining a good momentum resolution.

Its active volume of 90 m^3 is filled with an Ar and CO_2 mixture, which will be ionized by charged particles flying through it. There is a high voltage cathode in the middle of the active volume, which generates an electric field causing free electrons produced in the ionization to drift towards the end-plates. These end-plates consist of the readout chambers of the TPC, which are multi-wire proportional chambers with cathode pad readout, where the signal of incoming electrons is amplified and then registered by the readout pads. The geometry of the readout chambers and the readout pads below make it possible for one track to have up to 159 TPC clusters, where the 2D space point is determined by the pad position and the third dimension can be calculated from the drift time of the freed electron. The TPC also measures values for the mean energy loss dE/dx of the traversing particle, which is needed for PID, as will be explained in section 2.3.

²The impact parameter is the *Distance of Closest Approach* of tracks to the primary vertex and is also called DCA.

2.2.3 The Time-Of-Flight (TOF) detector

The TOFs main purpose is to complement the PID process for charged particles in the intermediate momentum range (below 2.5 GeV/c for pions and up to 4 GeV for protons). It consists of *Multi-gap Resistive-Plate Chambers* (MRPC), which determine the time of flight of a traversing particle by measuring the time between the event collision (which is measured by the T0 detector) and the TOF hit cluster. Its functionality is similar to that of the TPC: the sensitive gaseous volume inside the detector is ionized by traversing charged particles, however, the electrodes generating the electric field are very close together ($\mathcal{O}(10^{-3}\text{m})$) unlike the electrodes of the TPC ($\mathcal{O}(1\text{m})$), which means that there is essentially no drift time for the freed electrons, immensely increasing the time resolution.

2.3 Tracking and reconstruction

The track reconstruction in ALICE is accomplished by an inward-outward-inward approach [10]: After a preliminary position of the primary vertex was estimated from the signal of the SPD layers, it is used together with clusters at high radius in the TPC to built track seeds. These seeds are then propagated inwards and the track parameters are updated with each new found cluster using a Kalman Filter. If tracks have less than 20 of a maximum of 159 TPC clusters or they have missed more than 50% of their expected clusters, they are rejected and not further considered. For the other tracks a preliminary PID will be performed by using the energy loss measurements by the TPC. For this, the specific mean energy loss by ionization for particles with charge z traversing a medium with atomic number Z and mass number A

$$\left\langle -\frac{dE}{dx} \right\rangle = K z^2 \frac{Z}{A} \frac{1}{\beta^2} \left[\frac{1}{2} \ln \frac{2m_e c^2 \beta^2 \gamma^2 W_{max}}{I^2} - \beta^2 - \frac{\delta(\beta\gamma)}{2} \right] \quad (2.3)$$

is utilized ([11], page 447). Here, m_e is the electron mass, W_{max} the maximal energy transferred to an electron in a single collision, I is the mean excitation energy and $\delta(\beta\gamma)$ is a correction factor. This expression is called the Bethe-Bloch-formula and it does not explicitly depend on momentum, but it is among other things dependent on the relativistic factors β and γ :

$$\beta = \frac{v}{c}, \quad \gamma = \frac{1}{\sqrt{1 - \beta^2}} \quad (2.4)$$

Since these factors only depend on the velocity, particles with different masses have different momenta at equal β and γ (and therefore equal mean dE/dx). Figure 2.4 shows how this can be used to identify particles: the momentum of a given track can be obtained from its curvature and the dE/dx measurement can then be used to assign the track to the corresponding band. With this, the tracking algorithm assigns a mass hypothesis³ to each remaining track, which will be used in the subsequent steps of the track reconstruction process. After the tracks have been propagated to the inner radius of the TPC, the path will be prolonged to the outer

³This mass hypothesis is not the final PID, as most analyses will do a separate identification using the parameters of the fully reconstructed tracks.

ITS layer using the PID hypothesis and if a matching cluster is found, it will be used as the starting point⁴ of the reconstruction in the ITS, which follows a similar inward procedure as in the TPC. Then, the tracks from ITS and TPC are combined and the second stage of the tracking commences: now, a Kalman filter is used to refit the ITS+TPC tracks outwards, where the track parameters are updated at each step. After reaching the end of the TPC, the tracks are attempted to be matched with signals from the *Transition Radiation Detector* (TRD), the TOF and, if possible, are extrapolated to the *Electromagnetic Calorimeter* (EMCal), the *High Momentum Particle Identification Detector* (HMPID) and the *Photon Spectrometer* (PHOS). The last step of the tracking consists of one last refit from the TRD all the way inwards to the innermost ITS layer. With this, all the final track properties⁵ and the covariance matrices for each track are determined, which will be saved and can then be used for analysis.

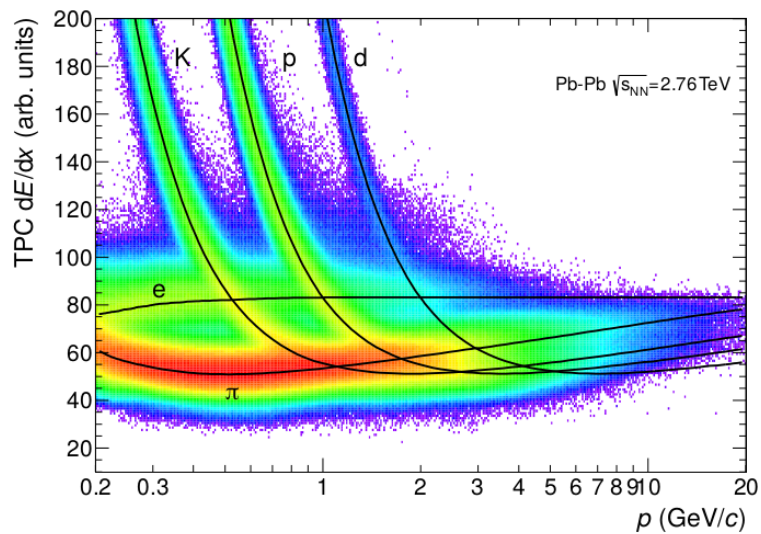


Figure 2.4: The specific energy loss of different particle species in the TPC during heavy-ion collisions. The black lines indicate the expected mean values for different particles. (Taken from [12])

⁴The algorithm also tries to find standalone tracks in the ITS

⁵with energy loss correction already taken into account

Chapter 3

Analysis tools

The main objective of this thesis is to assess to what extent it is possible to use the data collected by ALICE to measure the mass of ${}^3_{\Lambda}H$ and to study what resolution can be expected in such a measurement. As mentioned before, the focus will lie on candidates that have decayed via the 3-body decay channel and they will be reconstructed using the *KFparticle vertexing package* (KF package).

A dataset produced by a *Monte Carlo* (MC) simulation will be studied to determine kinematic regions in which the mass measurement is expected to be most accurate. This dataset will also be used to investigate possible candidate selections that are necessary to reduce combinatorial background in real data. The next sections will give a quick overview of the specific software used for this analysis.

3.1 The KFparticle vertexing package

The KF package utilizes the *Kalman-Filter* method to fully reconstruct short lived particles that decayed inside ALICE after being produced during a heavy-ion collision. A Kalman-Filter is a mathematical tool used to solve fit problems and it is already utilized in ALICE for event reconstruction and tracking. In contrast to other vertexing packages, the KF package allows the reconstruction of decayed particles while simultaneously producing a direct estimate of not only the position of the primary and secondary vertices, but also of the reconstructed particles momentum, energy and proper decay time, together with the covariance matrix [16].

In general, a Kalman Filter combines a mathematical model describing the evolution of a system with measurements, which will be taken into account by the model to improve its predictions. The basic steps the KF package follows to reconstruct decayed particles are as follows ([16], [18]):

- A first approximation of the secondary vertex coordinates is made using all daughter tracks
- One daughter is transported to these coordinates and its momentum and the covariance matrix at that point are calculated
- The properties of this daughter are used as measurement to update the properties of the mother particle (filter step)
- This is repeated for all daughters

An in-depth mathematical description of this process can be found in [16]. The KF package has already been tested for analyses in heavy-flavor physics ([20], [18]) and is also expected to be useful for the investigation of hypernuclei.

3.2 Monte Carlo Sample

The simulated MC sample used in this thesis was generated using the *Heavy Ion Jet INteraction Generator* (HIJING), v1.36.1 [23]. The used transport code, which simulates the detector response for each generated event, is called GEANT4 v10.4.2 [2] and it is anchored to LHC18q pass1¹.

All the generated events are simulated Pb-Pb collisions at a center-of-mass energy per nucleon pair of $\sqrt{s_{NN}} = 5.02$ TeV. In each generated event a certain amount of signal was injected which is summarized in table 3.1. The signal was injected "flat" in transverse momentum and rapidity y , which means that the injected particles are uniformly distributed over the p_T -range from 0 GeV/ c to 10 GeV/ c and over the rapidity range of $|y| < 1$. Since particles created in actual collisions will not be uniformly distributed over this p_T -range, the candidates in the MC sample are reweighted using a phenomenological model for the production of hadronic matter, which was published in [1]. This is visualized in figure 3.1, where the unmodified distribution of reconstructed transverse momenta of the candidates is compared to the reweighted one. The reweighting is done using the transverse momentum generated by the MC simulation.

The MC dataset consists of 120.000 events generated at 0-10% centrality and 400.000 events each at 10-50% and 50-90% centrality, where centrality is a commonly used variable for categorizing collision events. It is defined as a percentage of the total hadronic interaction cross section in Pb-Pb collision σ_{PbPb} . It can be expressed via the impact parameter b , which is the distance of the centers of two colliding nuclei in the plane transverse to the beam direction [12]:

$$c(b) = \frac{1}{\sigma_{PbPb}} \int_0^b \frac{d\sigma}{db'} db'. \quad (3.1)$$

¹This is important so the detector configurations are the same in the MC sample and the collected data.

Since b is not experimentally measurable, the centrality can be approximated as the fraction of cross section with the largest detected charged-particle multiplicity N_{ch} [12]:

$$c \approx \frac{1}{\sigma_{PbPb}} \int_{N_{ch}}^{\infty} \frac{d\sigma}{dN'_{ch}} dN'_{ch}. \quad (3.2)$$

MC sample: Injected signal per event		
Species Name	Symbol	Injected amount
Deuteron	2H	10
Triton	3H	10
Helium-3	3He	10
α -Particles	α	10
Hypertriton	${}^3_{\Lambda}H$	40
Hyper-hydrogen-4	${}^4_{\Lambda}H$	20
Hyper-helium-3	${}^4_{\Lambda}He$	20

Table 3.1: Signal that was injected in each simulated event generated by HIJING. An equal amount of anti-particles of each species was also injected into each event.

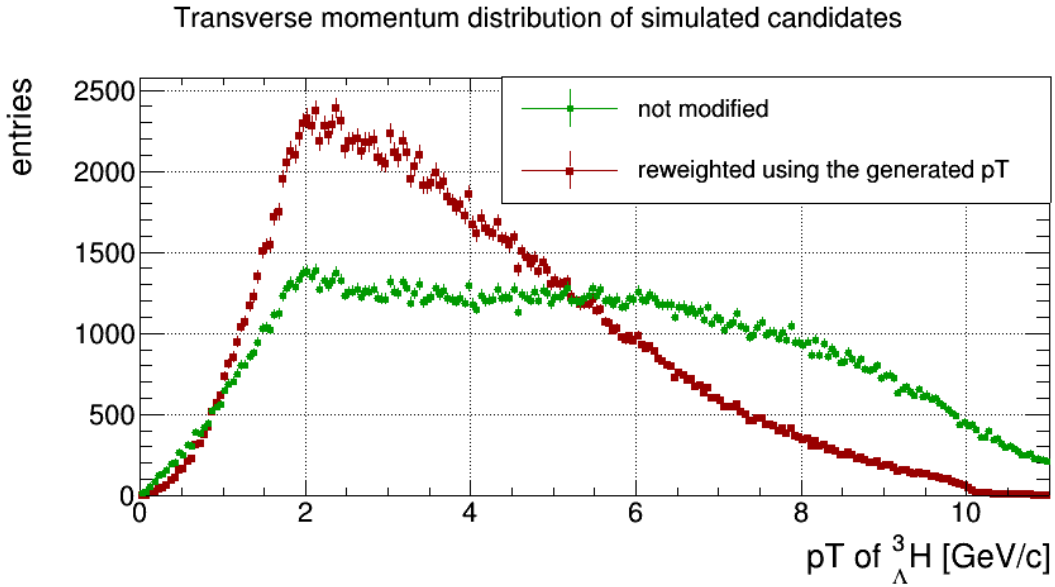


Figure 3.1: Reconstructed transverse momentum p_T of the candidates generated in the MC simulation. The reweighting is done with a phenomenological model published in [1].

3.2.1 Preselections for the MC dataset

The data is analyzed using ROOT, which is an open-source analysis framework often used for high-energy physics. Some basic candidate selections have already been implemented in the MC simulation with the goal to ensure a good track reconstruction and a realistic representation of data. They are summarized in following tables: table 3.2 shows the selections that apply to all tracks. The *TPC refit* flag of a track indicates if the last step in the tracking algorithm has been successful for this track. Requiring this to be true filters many low quality tracks. A kink topology is defined as a track, which, at some point, changes its direction seemingly without a reason, indicating a weak decay involving a neutral particle, which is not measurable by the ITS or the TPC (e.g. $K^\pm \rightarrow \mu^\pm + \nu_\mu$) [22]. Tracks with this property are rejected, since tracks involved in the Λ^3 -decay are not expected to show this behavior. χ^2 is a variable for describing how well a fit agrees with the measured points used for fitting (see 4.2). The selection includes a requirement on the TPC-specific χ_{TPC}^2 , divided by the number of clusters in the TPC, which is also required to be above a certain threshold to ensure particles have traversed a large part of the TPC. Furthermore, the pseudo-rapidity η is required to be within the acceptance of the TPC and the number of TPC clusters used for PID is required to be above 50 to ensure decent track quality.

The $n\sigma$ variable is often used in analyses with ALICE data and is defined as

$$n\sigma^i = \frac{S_{measured} - S_{expected}^i}{\sigma_{expected}^i} \quad (3.3)$$

where $S_{measured}$ is the signal that was measured for this daughter track, $S_{expected}^i$ is the signal that the particle species i is expected to produce and $\sigma_{expected}^i$ is the expected detector resolution for this species [22]. This variable is defined in a way that a $n\sigma^i$ -distribution containing exclusively particles of the species i will be gaussian, which means that requiring $n\sigma^i \leq 3$ should only reject about 0.3% of particles of the species i , which is why all daughter tracks need to fulfill this criterion for the TPC. Since it is not very likely for low momentum particles to reach the TOF detector, selections involving the $n\sigma_{TOF}$ variable only apply to daughters above certain momentum threshold. On top of that, the transverse momentum for each daughter is limited to the specified ranges.

Table 3.3 shows the criteria with which the reconstructed candidates are selected. The mass of a candidate must be in the indicated range and the $\Lambda^3 H$ -candidate track's *Distance of Closest Approach* (DCA) to the primary vertex is required to be smaller than 5 cm (to ensure that the track originates in the beam pipe). The cosine of the pointing angle α must be larger than 0.999, where α is defined as the angle between the continuation of the line connecting the primary and secondary vertex and the vector of the sum of the daughter momenta.

Lastly, the χ^2/NDF value of the candidate reconstruction with the KF package is required to be ≤ 20 , while the *Number of Degrees of Freedom* (NDF) associated with this reconstruction has to be above 0.

Track selection		
Species	Variable	Selection
All	TPC refit	True
All	Kink topology	reject
All	$\chi_{TPC}^2/nTPCclusters$	≤ 5
All	$ \eta $	< 0.9
All	nPIDclustersTPC	≥ 50
All	$n\sigma_{TPC}^i$	≤ 3
π	nTPCclusters	≥ 70
d	nTPCclusters	≥ 50
p	nTPCclusters	≥ 50
d	$n\sigma_{TOF}^d$	≤ 4 for $p_d \geq 1.5$ GeV/c
p	$n\sigma_{TOF}^p$	≤ 4 for $p_p \geq 1$ GeV/c
π	p_T	$0.1 \text{ GeV} \leq p_T \leq 1.2 \text{ GeV}$
d	p_T	$1.0 \text{ GeV} \leq p_T \leq 10.0 \text{ GeV}$
p	p_T	$0.4 \text{ GeV} \leq p_T \leq 5.5 \text{ GeV}$

Table 3.2: Basic selections applied for the daughter tracks from the MC simulation.

Candidate selection	
Variable	Selection
Candidate mass	$2.94 \text{ GeV}/c^2 \leq m_{\Lambda_H} \leq 3.05 \text{ GeV}/c^2$
$DCA_{\Lambda_H}^{PV}$	$\leq 5 \text{ cm}$
$\cos(\alpha)$	≥ 0.999
χ^2/NDF	≤ 20
NDF	≥ 0

Table 3.3: Basic selections applied for all reconstructed candidates from the MC simulation.

Chapter 4

Analysis and Results

4.1 Expected yield of ${}^3_{\Lambda}H$ in three-body decay

${}^3_{\Lambda}H$ is a rather rare particle with only around one being produced in the rapidity range $|y| < 0.5$ in 10^4 Pb-Pb collisions in the 0-10% centrality class [7]. Because of the low production rate and the low reconstruction efficiency (see section 4.5.2) of ${}^3_{\Lambda}H$, the yield of actual ${}^3_{\Lambda}H$ -particles in the available data is expected to be very limited. A rough estimate of this yield can be used to create sub samples of the MC simulation with a similar amount of candidates as expected for an actual measurement. This can be utilized to compare different models for fitting the measured mass distributions in a realistic manner (see section 4.2).

To obtain this estimate, the results published in [7] for the integrated ${}^3_{\Lambda}H$ - and ${}^3_{\Lambda}\bar{H}$ -yields dN_i/dy per event in the centrality class i (rapidity $|y| < 0.5$, $\sqrt{s_{NN}}=2.76$ TeV) were multiplied by the number N_{ci} of events recorded in 2018 in the respective centrality classes. The number of recorded events is $N_{c1} = 10^8$ events in the 0-10% centrality class and $N_{c2} = 1.5 \cdot 10^8$ events in the 10-50% centrality class. The contribution from events with 10-50% is expected to be slightly overestimated, since the yield per event decreases for more peripheral collisions and the results from [7] were obtained with a data sample that was uniformly distributed over the 10-50% centrality interval, while the dataset from 2018 contains $0.5 \cdot 10^8$ events in the 10-30% centrality class and 10^8 events in the 30-50% centrality class. The data from 2018 also includes $0.5 \cdot 10^8$ events in the 50-90% centrality class, however, because of the decrease of dN/dy for higher centrality, the contribution of these events to the overall yield is negligible.

The number obtained from this is then scaled by a factor $f_{BR} = 1.6$, since the branching ratio of the 3-body decay is 60% larger than that of the 2-body decay [14]. The reconstruction efficiency ϵ_{rec} for the 3-body decay, as well as the efficiency of the candidate selection ϵ_{sel} were estimated with the MC simulation in section 4.5.2, resulting in a factor $\epsilon_{sel}\epsilon_{rec} \approx 0.03$ ¹.

¹This number is a bit higher than the efficiency reported in section 4.5.2, since the candidate selection discussed there is not yet optimized. An optimized candidate selection is expected to have an efficiency higher than 3% across the p_T -range from 1 GeV/ c to 10 GeV/ c .

The resulting equation is:

$$N_{3body} = \epsilon_{sel}\epsilon_{rec} \cdot f_{BR} \cdot \sum_i N_{ci} \cdot \frac{dN_i}{dy} \Delta y \quad (4.1)$$

where dN_i/dy was assumed to be constant over the rapidity range $|y| < 0.5$ and thus $\Delta y = 1$. This calculation results in about 500 combined ${}^3_{\Lambda}H$ - and ${}^3_{\Lambda}\bar{H}$ -particles that can be successfully reconstructed and that will not be filtered out by the candidate selection. This estimate can be viewed as a lower limit, since a larger rapidity interval of $|y| < 0.9$ will be considered for this work and the center-of-mass energy per nucleon pair in each collision will be at $\sqrt{s_{NN}} = 5.02$ TeV instead of $\sqrt{s_{NN}} = 2.76$ TeV. These effects are expected to compensate for the overestimation arising from using a constant dN/dy for all events in the 10-50% centrality class in the 2018 data. In section 4.5, the amount of measured ${}^3_{\Lambda}H$ -particles in the transverse momentum interval $2 \text{ GeV}/c \leq p_T < 5 \text{ GeV}/c$ is 523, indicating that the 500 particles calculated with equation 4.1 could even be an underestimation.

4.2 Determination of the model used to fit the mass distributions

To accurately measure the mass of ${}^3_{\Lambda}H$ a good model for describing the mass distribution is necessary. Thus, in this section the performance of three different functions to fit the ${}^3_{\Lambda}H$ mass distributions will be compared. The chosen functions are symmetric and are motivated as follows:

A single Gaussian function: The formula of this function is given by

$$F_1(x) = n \cdot e^{-\left(\frac{1}{2} \frac{(x-\mu)^2}{\sigma^2}\right)} \quad (4.2)$$

where μ denotes the mean of the distribution, σ is the standard deviation and n represents a normalization factor. The single Gaussian function describes a lot of phenomena in physics and in nature, because it describes the random behaviour of statistical components when repeating one experiment a large number of times. Additionally, it has already been used to fit mass distributions of ${}^3_{\Lambda}H$, for example in [22]. This function has three free parameters.

A double Gaussian function: This function is the result of adding two of the previously described Gaussian functions:

$$F_2(x) = n_1 \cdot e^{-\left(\frac{1}{2} \frac{(x-\mu_1)^2}{\sigma_1^2}\right)} + n_2 \cdot e^{-\left(\frac{1}{2} \frac{(x-\mu_2)^2}{\sigma_2^2}\right)} \quad (4.3)$$

All the variables are defined as in equation 4.2. Because of the long lifetime of ${}^3_{\Lambda}H$, the distance between primary and secondary vertex can vary strongly: the secondary vertex could be close to the beam pipe for some candidates and behind the last ITS layer for others. This causes a strong variation in mass resolution across all candidates. The double Gaussian function makes it possible to include two mean resolution values. This is why it is expected to perform equally good or better than the single Gaussian function, which only uses one resolution for the whole distribution. The mass distribution is expected to be symmetric, which is why $\mu_1 = \mu_2 = \mu$ is used. This constraint leaves this function with five free parameters.

A Voigt distribution: The last function is a Voigt distribution, which results from convoluting a Breit-Wigner distribution with a Gaussian:

$$F_3(x) = n \cdot \int_{\mathbb{R}} e^{-\left(\frac{1}{2} \frac{(\tau-\mu)^2}{\sigma^2}\right)} \cdot \frac{\gamma}{\pi((x-\tau)^2 + \gamma^2)} d\tau \quad (4.4)$$

Here, γ denotes the width of the Breit-Wigner part of the Voigt function, while the other variables are defined as described above (equation 4.2). In the case of the ${}^3_{\Lambda}H$, the Voigt function could describe its peak shape, since the natural distribution of ${}^3_{\Lambda}H$, which is assumed to follow a Breit-Wigner curve, is convoluted with detector effects, which, in the simplest case, should be described by a Gaussian. However, if one tries to confirm this motivation, it can be seen in figure 4.1 that the Breit-Wigner function does not perfectly describe the true mass distribution generated by

the MC. Furthermore, the intrinsic width γ of the Breit-Wigner part of the Voigt distribution in fits like the ones shown in figure 4.2 does not correspond to the width shown in figure 4.1. Due to the long lifetime of the ${}^3_{\Lambda}H$ and the relation $\tau = \frac{\hbar}{\Gamma}$, with τ being the lifetime and Γ the intrinsic width of the resonance, the peak of the true mass distribution is so narrow that the Breit-Wigner part of equation 4.4 essentially acts as a δ -function compared to the detector resolution (see figure 4.4 later in this section). Even though the originally assumed motivation for the use of the Voigt function does not seem to be correct, the results that will be presented in this section show that it is still interesting to include this function in the comparison. The Voigt function has four free parameters.

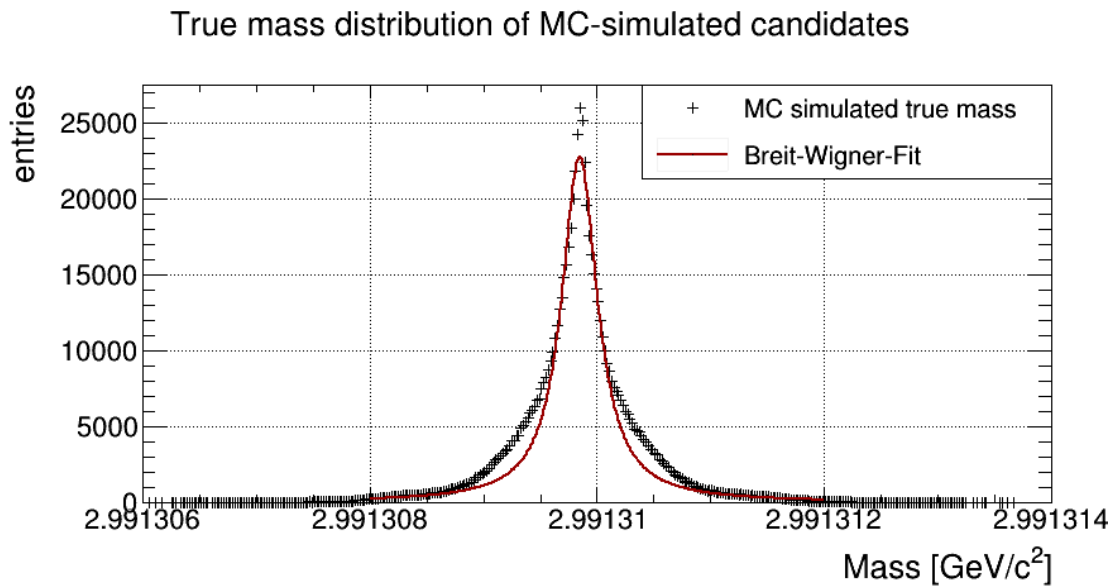
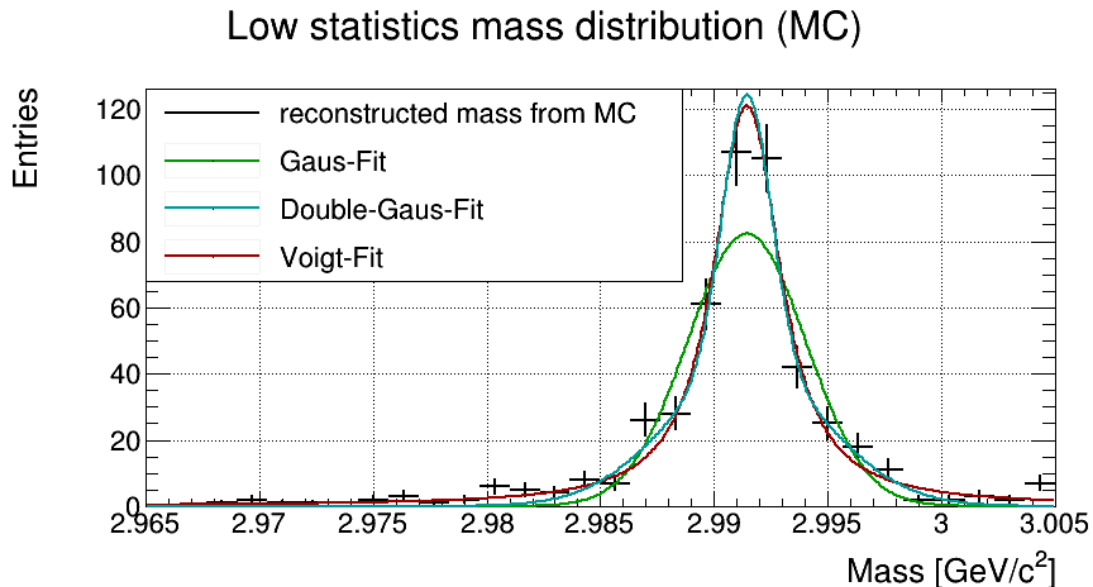
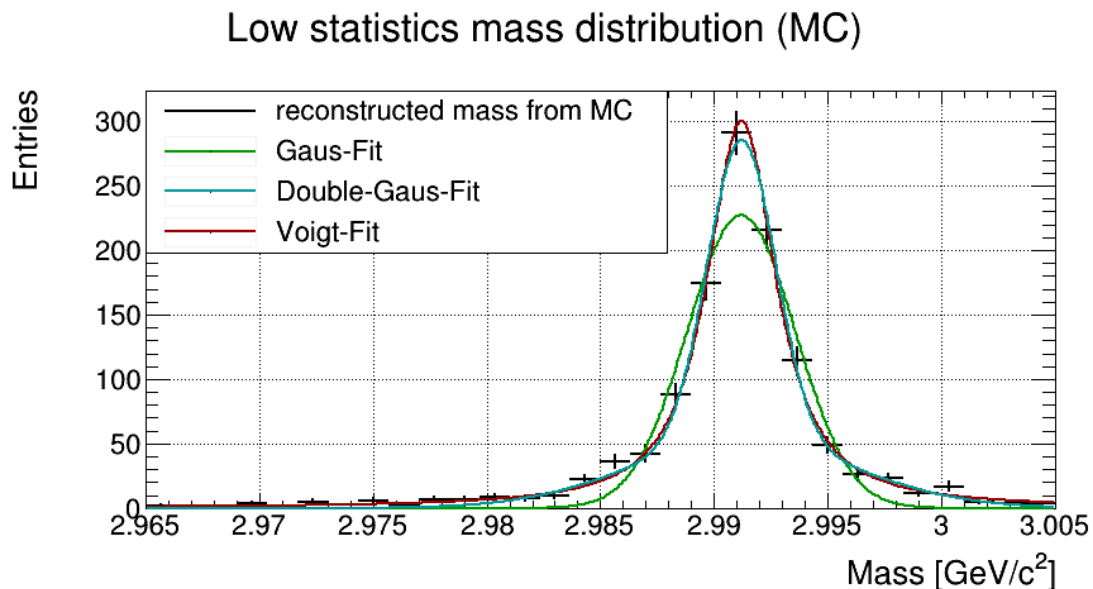


Figure 4.1: Breit-Wigner fit to m_{true} distribution.



(a) different fits for 500 candidates



(b) different fits for 1200 candidates

Figure 4.2: Examples of fits of mass distributions from the conducted simulated experiments. The resulting χ_{red}^2 values of each fit are extracted and the χ_{red}^2 values of all simulated experiments are summarized in figure 4.3.

The suitable choice of the fitting function might be sensitive to the number of candidates contained in the measured distribution, so in this investigation it was attempted to create similar circumstances as in real data using the MC data: a number of simulated experiments was performed, where a given amount of MC simulated candidates were selected and fitted with the above mentioned functions. As indicated in section 4.1, we expect at least 500 candidates fulfilling the selection criteria. This estimate was used as a starting point for the choice of the different candidate amounts. Examples for two of these experiments with different candidate counts can be seen in figure 4.2.

The used fit algorithm utilizes the *least square method*, which aims at minimizing the sum

$$\chi^2 = \sum_{i=1}^k \left(\frac{y(i) - f(x(i))}{e(i)} \right)^2 \quad (4.5)$$

where $y(i)$ is the number of entries in mass bin i with k being the total number of bins inside the fit range (in this case 2.98 GeV - 3.00 GeV), $f(x(i))$ is the value of the fit function at the center of each bin and $e(i)$ is the uncertainty on each bin count (in this case $e(i) = \sqrt{y(i)}$ is used). To compare χ^2 -values of different fits and different numbers of bins k , the reduced χ^2

$$\chi_{red}^2 = \frac{\chi^2}{n_{ndf}} \quad (4.6)$$

is used. n_{ndf} is the number of degrees of freedom, which is the number of bins k subtracted by the number of free parameters of the fit. A fit with a function that is a suitable model for the distribution should result in $\chi_{red}^2 \approx 1$, if the uncertainties of the distributions are realistic.

In every conducted virtual experiment, the χ_{red}^2 -value of each fit was extracted and the results are summarized in figure 4.3.

Looking at figure 4.2, one can already see that the single Gaussian function does not describe the distribution very well, as it does not peak as sharply as the MC candidate distribution and goes towards zero too quickly to catch the tails, while both other functions do not seem to have these issues in this example. This seems to be the case for most carried out virtual experiments, as can be seen in figure 4.3, where the result of the Voigt fit tends to have the lowest χ_{red}^2 value, with a peak at around one. While the χ_{red}^2 -distribution of the double Gaussian function peaks in the same region, it has more entries at higher χ_{red}^2 values. The χ_{red}^2 -values of the single Gaussian fit are almost always significantly larger while looking at a smaller number of candidates, but they get shifted to even larger values with more candidates, even though a larger sample of candidates should mean a better agreement of model and data (if the model is correct). This indicates that the single Gaussian function should not be used to fit mass distributions of ${}^3_{\Lambda}H$.

In figure 4.4, the described investigation was repeated and this time, the width γ of the Breit-Wigner part of the Voigt function was fixed to the value extracted from the fit in figure 4.1. It can be observed that the Voigt function now behaves exactly like the single Gaussian function, which shows that the Breit-Wigner part in equation 4.4 acts as a δ -function when using realistic values for γ .

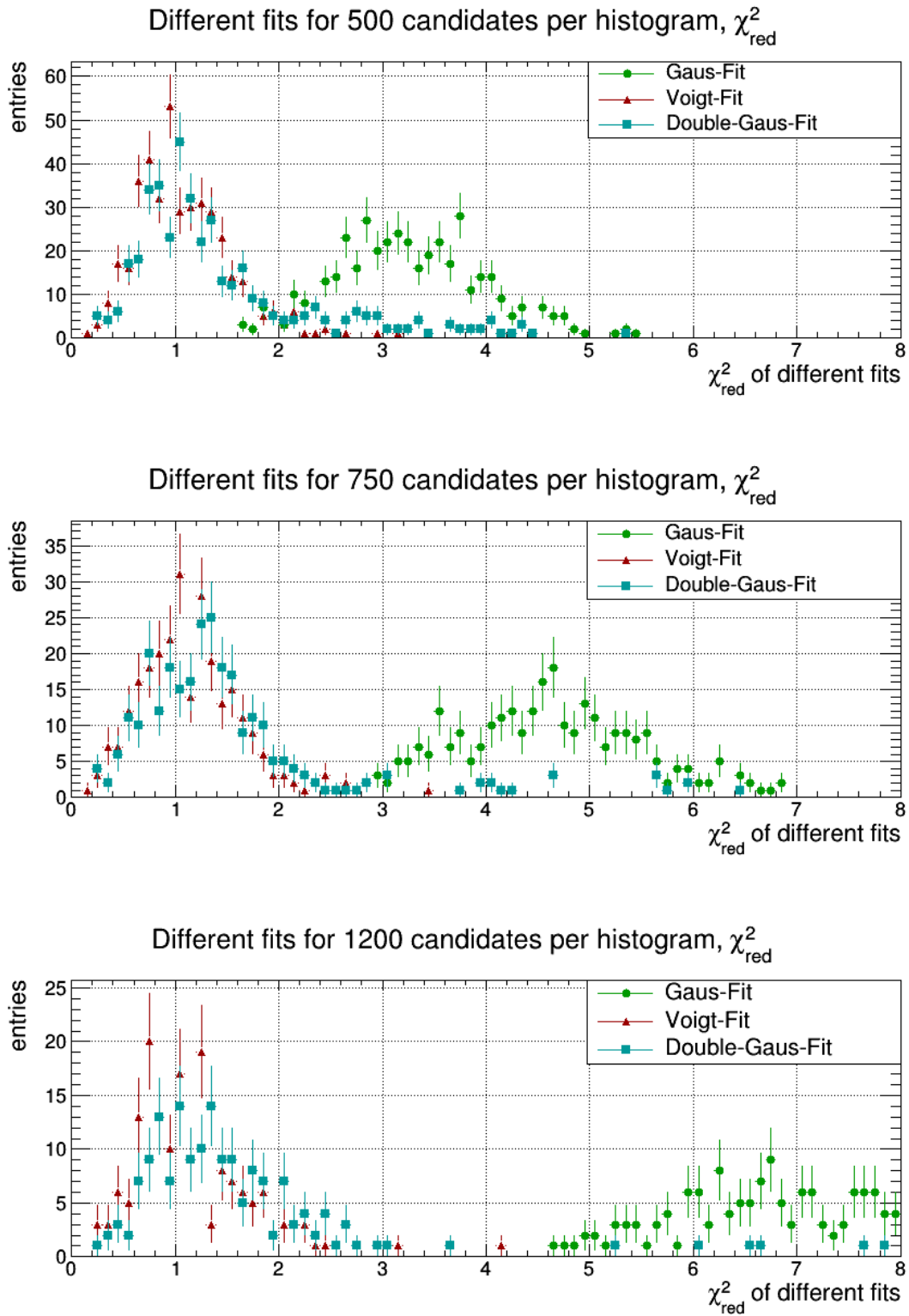


Figure 4.3: χ^2_{red} of fit results using different fit functions and different numbers of candidates

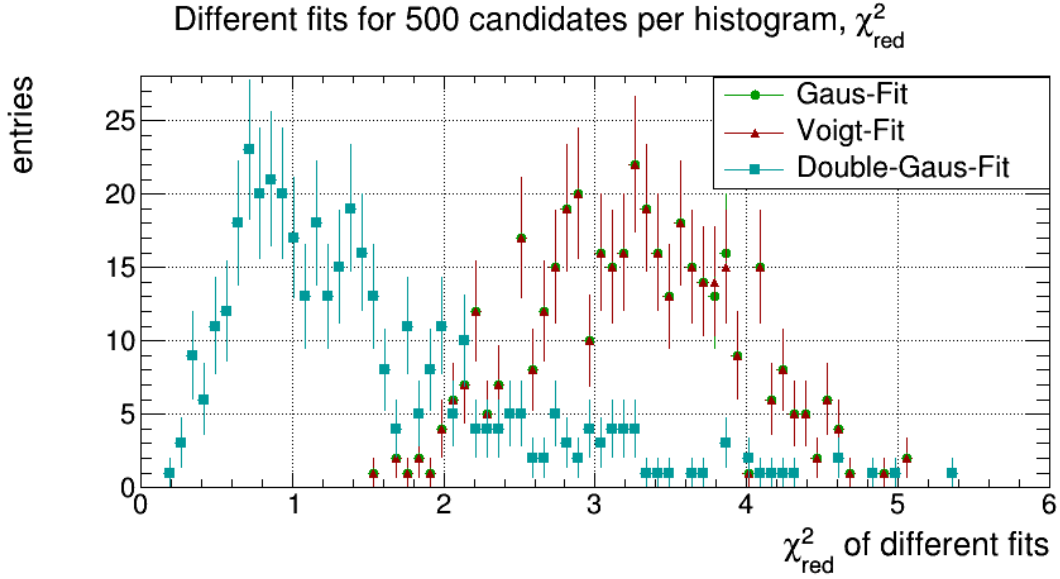


Figure 4.4: χ_{red}^2 of fit results while the width of the Breit-Wigner part of the Voigt function is fixed to the value extracted from figure 4.1.

According to this investigation it seems reasonable to use the Voigt function for future fitting processes, because the χ_{red}^2 -values are consistently small, while having only four instead of the five free parameters of the double Gaussian function. Furthermore, the fit with the Voigt function converges more consistently, especially for the simulated experiments with 500 candidates. Here, the fit with the Voigt function failed to converge in 4 of the 417 conducted experiments, while the double Gaussian function did not converge in 11 cases. Another reason for the usage of the Voigt function instead of the double Gaussian function is that it is possible for the double Gaussian function to return an unphysical result, for example the one shown in figure 4.5: if one does not restrict the possible values for σ_1 and σ_2 in equation 4.3, their values can be so different that the resulting function does not properly describe the mass distribution anymore. The algorithm still converges, in this case with a reasonable χ_{red}^2 -value of 1.92, but the result cannot be used for further analysis. As discussed before (see figure 4.4), using drastically different values of σ and γ in equation 4.4 results in a single Gaussian function (or a Breit-Wigner function for $\sigma \ll \gamma$), which shows that the described issue cannot occur when using a Voigt function.

In conclusion, the use of the Voigt function still lacks physical reasoning, however, it describes the shape of the mass distributions reasonably well, while also not having the mentioned issues of using the double Gaussian function. How exactly the reconstruction produces the observed shape needs to be looked into in the future. There are a lot of factors that could have an impact on this, from physical detector effects in the ITS and the TPC to changes of the peak shape during data processing in the tracking algorithm or the final reconstruction with the KF package. The double Gaussians can be used to determine systematic uncertainties.

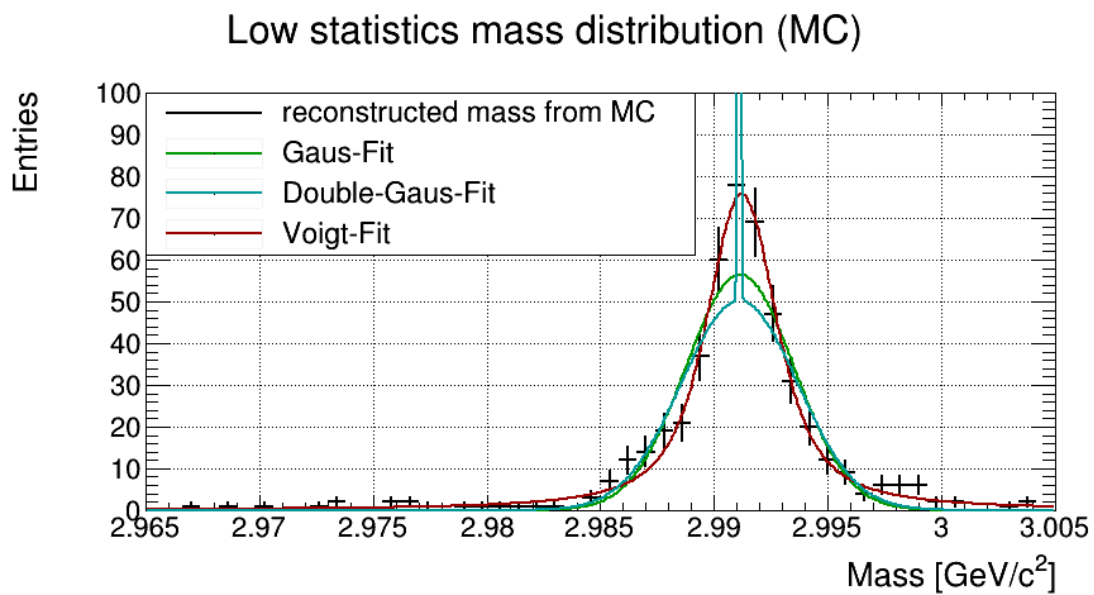


Figure 4.5: Example of fits of a mass distribution created in one of the simulated experiments. For the fit with the double Gaussian function, the fit algorithm converged, but the result can not be considered physical, since part of the resulting fit function does not behave reasonable.

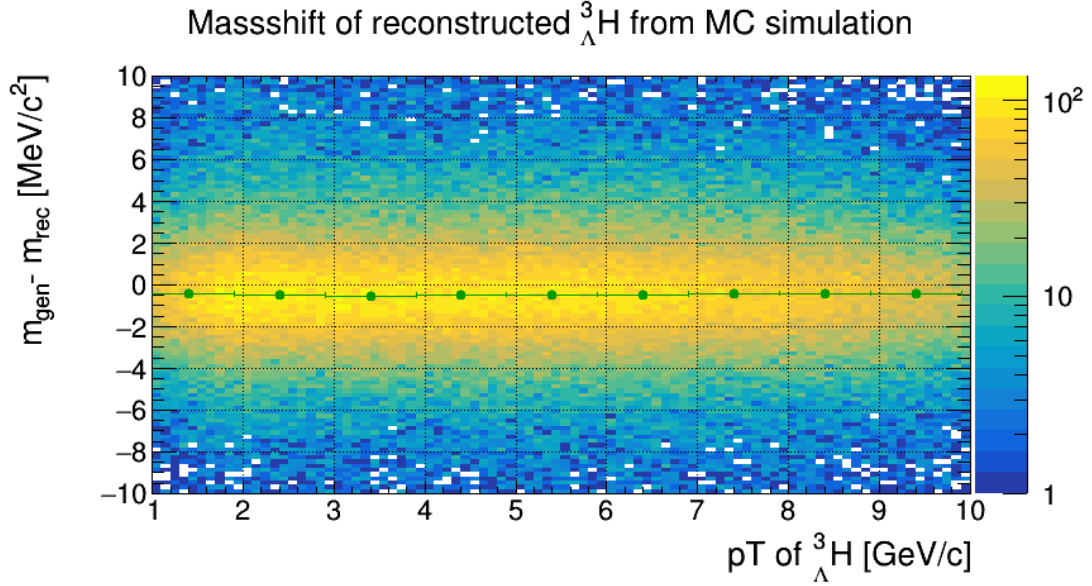
4.3 Systematic mass shift introduced by the KF particle package

Additionally to knowing how to accurately extract the mass of the ${}^3_{\Lambda}H$ from a given distribution, one needs to ensure that this mass reflects the value that was used for the simulation. Since the exact mass value with which ${}^3_{\Lambda}H$ -particles are inserted into the MC simulation is known (currently $m_{gen} = 2.991\,31$ GeV), the reconstructed mass values m_{rec} can be verified. This can be seen in figure 4.6, where the difference between the generated mass and the mass reconstructed by the KF package is visualized. The figure shows that the masses of the candidates are systematically reconstructed around 400 keV higher than the value from the MC simulation.

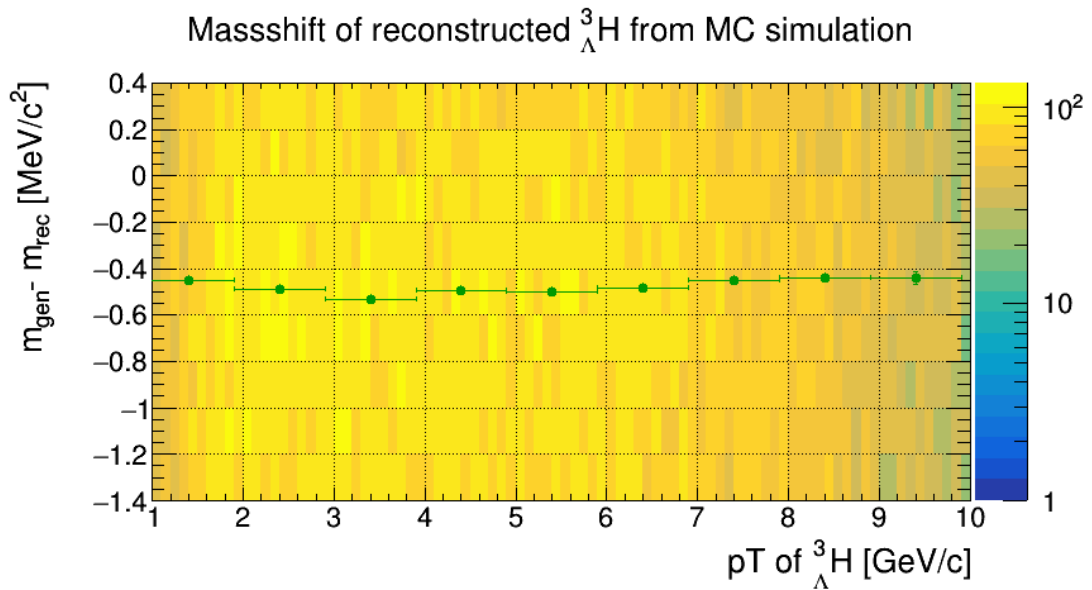
To check where in the reconstruction this shift occurs, the mass of the ${}^3_{\Lambda}H$ -candidates were calculated directly from the track momenta before they are modified by the KF package. The result of this is shown in figure 4.7, where it can be seen that the mass shift is significantly smaller for the values determined without the KF package. The larger peak width of this distribution as well as the slight shift of around 70 keV are assumed to arise from the fact that for this calculation, the used daughter momenta are still the ones resulting from the propagation towards the primary vertex during the track reconstruction, instead of the momenta at the secondary vertex that are calculated during the candidate reconstruction with the KF package.

From this plot it can be concluded that the systematic mass shift happens during the kalman filtering process. An investigation following up this result has revealed inconsistencies in the mass values of the daughters used in the KF package and the ones used in the MC simulation: the mass of the deuteron showed a discrepancy of around 500 keV between the two algorithms ($m_{KF} = 1.876\,124$ GeV and $m_{MC} = 1.875\,613$ GeV) and the mass of the proton also differed slightly. This issue has since been fixed, as can be seen in figure 4.8. Updating the masses of the daughters to the most recent values reported in "CODATA Recommended Values of the Fundamental Physical Constants: 2018"² has eliminated the large systematic mass shift that was occurring for ${}^3_{\Lambda}H$ -candidates reconstructed by using the old version of the KF package. The small mass shift that is still remaining will be addressed in the following sections.

²most importantly, the mass of the deuteron has been set to $m_d = 1.875\,613$ GeV



(a) full mass shift range



(b) enlarged

Figure 4.6: The systematic mass shift across the whole p_T -range in MC simulated data. The 2D histogram has been projected onto the Y-axis for different p_T -ranges and the projections were fitted with the Voigt-Function. The green points show the mean value of the Voigt function for each fit. The average χ_{red}^2 -value of all fits is $\chi_{red}^2 = 1.6$.

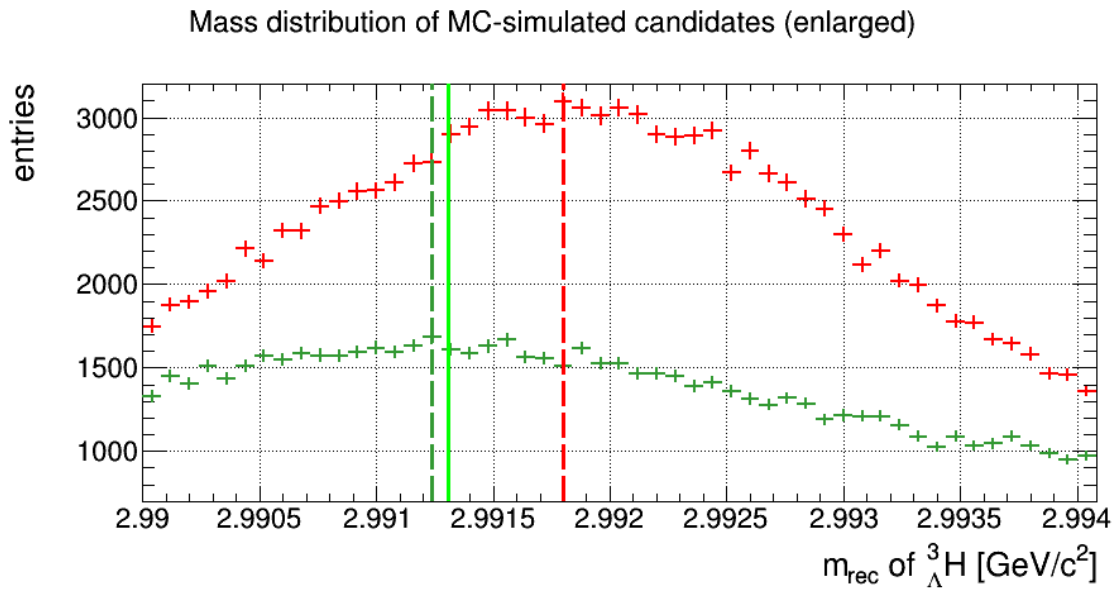
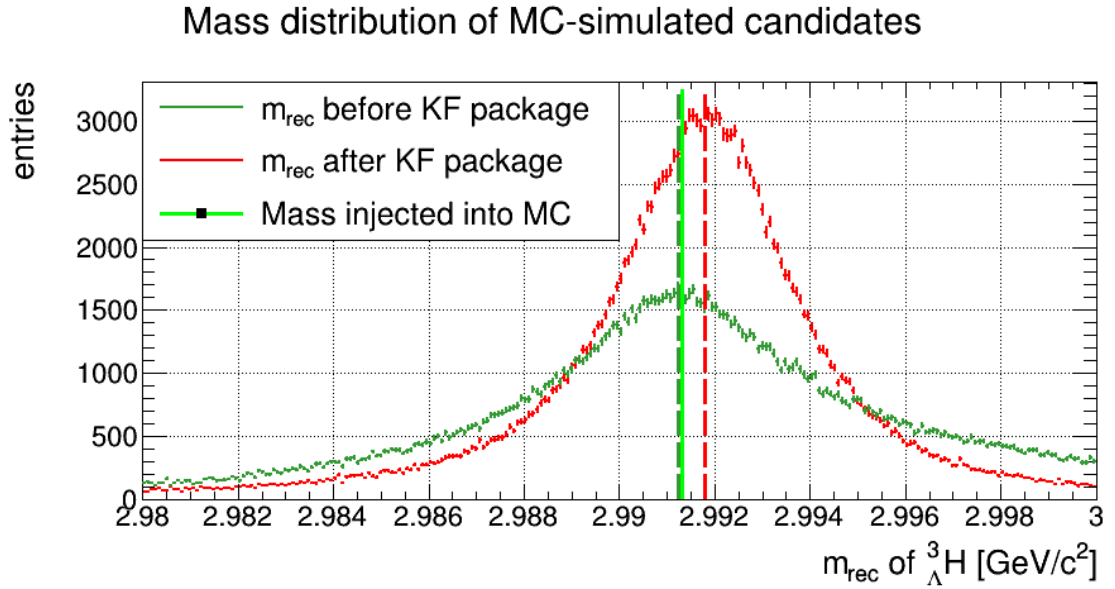


Figure 4.7: A comparison of the mass distribution obtained by the KF package and the one calculated directly from the daughter momenta. The peak positions are indicated by the dashed lines, whereas the mass used in the MC simulation is shown by the bright green line.

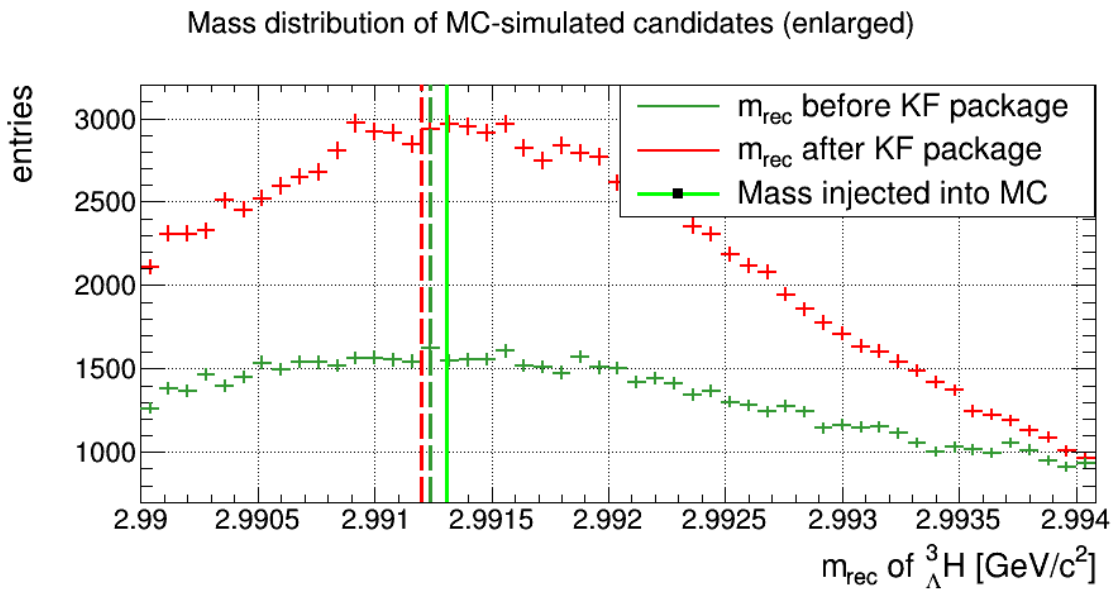
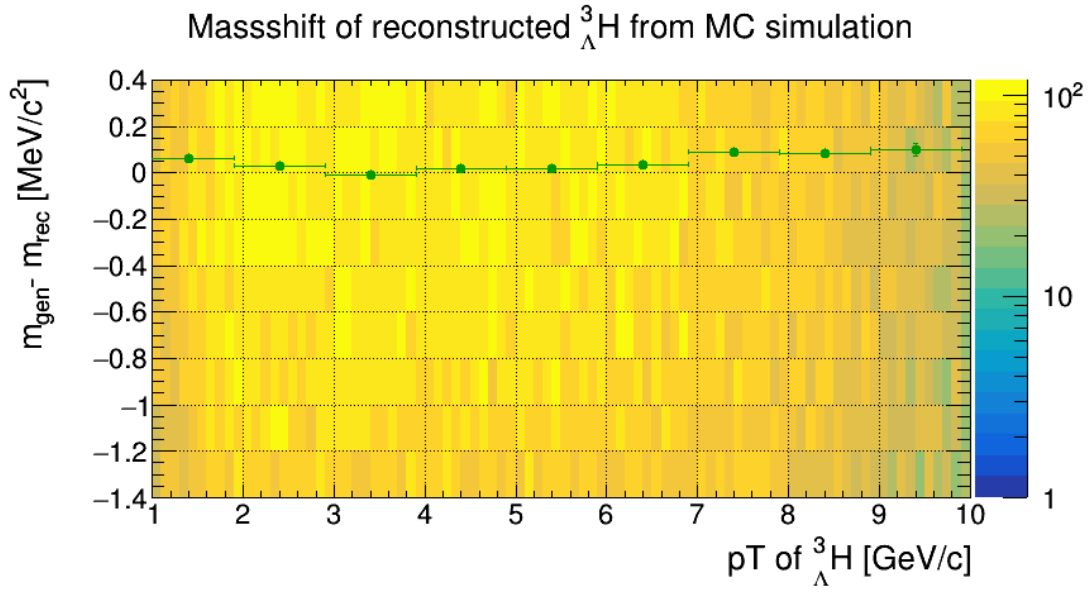


Figure 4.8: The investigations that were done to obtain figure 4.6 and 4.7 were repeated with consistent mass values for the daughters in the KF particle package and in the MC simulation.

4.4 Wrongly assigned hits in the ITS

${}^3_{\Lambda}H$ -candidates are reconstructed using the tracks that were obtained by the tracking algorithm, which searches for matching clusters and combines them to complete tracks (see section 2.3). Due to the high track density in the ITS it can happen that ITS-clusters in layers before the decay point of a ${}^3_{\Lambda}H$ -candidate are assigned to the track of a daughter, since its trajectory fits to the cluster within uncertainties. However, the daughter comes from the secondary vertex and therefore could not have crossed this ITS layer (as is illustrated in 4.9). These wrongly assigned hits (*fake hits*) artificially prolong the tracks and the energy loss correction, which depends on how much of the detector a particle has traversed, is overestimated, which distorts the track momenta. Additionally, the fake hits could slightly alter the track geometry, if clusters at the edges of the allowed uncertainties are wrongly assigned, which also influences the track momenta.

In figure 4.10 the share of candidates with fake hits in the daughter tracks³ are shown, together with the radii of the different ITS layers. The plot indicates that almost all of the candidates which decay right after one of the first 3 ITS layers contain fake hits. In these cases, it is assumed that the fake hits come from clusters caused by the candidates themselves: when a candidate decays right after crossing an ITS layer and producing a signal inside it, all the daughter tracks originate very closely to this signal, which makes it likely for the algorithm to wrongly assign the produced cluster to one or more of the daughter tracks.

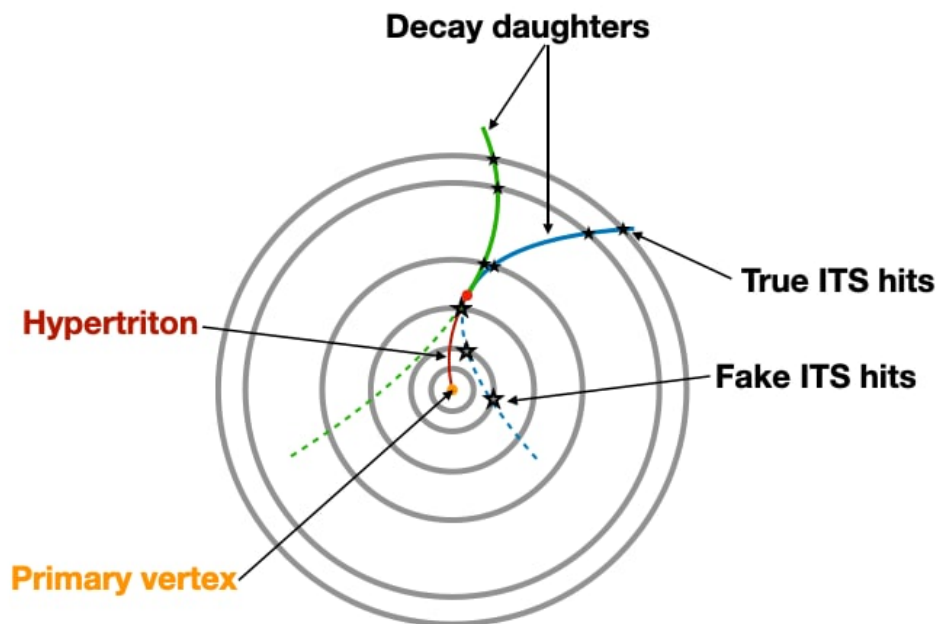


Figure 4.9: Illustration of the definition of "Fake Hits". The picture shows a cross section of the ITS with a hypertriton decaying via the 2-body decay channel. (Picture by Sebastian Hornung)

³The ${}^3_{\Lambda}H$ -candidate itself can't have fake hits, since it is assumed to originate from the primary vertex. From here, when a "candidate with fake hit" is mentioned, it is to be understood as "candidate that was reconstructed from daughter tracks containing wrongly assigned ITS hits".

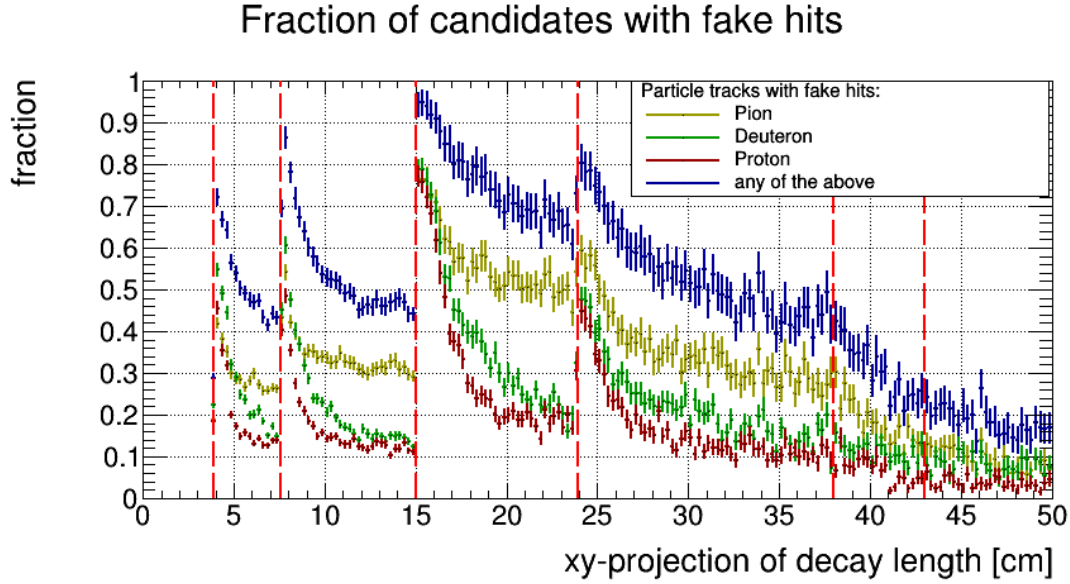


Figure 4.10: Share of candidates for which the daughter tracks have fake hits over the xy -projections of the decay length of the mother. The inner radii of the ITS layers are indicated by the red dashed lines.

The momentum of each candidate is mostly inherited by the deuteron originating from the decay, since it is the heaviest particle of the produced daughters. It is assumed that in some cases this causes the deuteron track to look similar to the continuation of the candidate track. Because of this, deuteron tracks are more likely to have fake hits originating from the candidate itself, even if it doesn't decay right after an ITS layer, which is why the amount of deuteron tracks with fake hits does not fall off as quickly as for the proton tracks after each ITS layer.

For pions, the exact opposite should be the case: as the pion is significantly lighter than deuterons or protons, the angle between the daughter track and the candidate track is expected to be larger for the pion tracks than for the other two. Because the candidate track originates from the primary vertex, its xy -projection is likely to be approximately perpendicular to the ITS layers it crosses. Because of this and the larger expected angle between pion- and candidate track, the angle between the inward prolongation of the pion track and the ITS layers crossed by the candidate should on average be shallower than for the other two tracks⁴. A shallower angle between a track and an ITS layer means that during the inward propagation a larger volume of this layer will be checked for matching clusters, increasing the probability of assigning a fake hit. This could be an explanation for the high observed amount of pion tracks containing fake hits, but it will need further investigations to prove or refute this, as this effect has not yet been studied in detail.

Figure 4.11 illustrates the influence the fake hits have on the position of the mass peaks. At $p_T > 4 \text{ GeV}/c$, when filtering all candidates with fake hits, the overall mass shift seems to be overcompensated, as the reconstructed candidates tend to have a higher mass than the MC value when using this restriction. From figure 4.10 and table 4.1, where the percentages of candidates with fake hits are reported, it is

⁴especially at low rapidity, where the candidate track and its xy -projection are approximately equal

also clear that rejecting all candidates with fake hits means a substantial loss in the amount of candidates that can be measured (around 40%). However, the influence the fake hits have in the mass measurement can still be utilized to improve its accuracy. For this, two different approaches were investigated, which had the goal to reduce the amount of rejected candidates and to lower the mass shift.

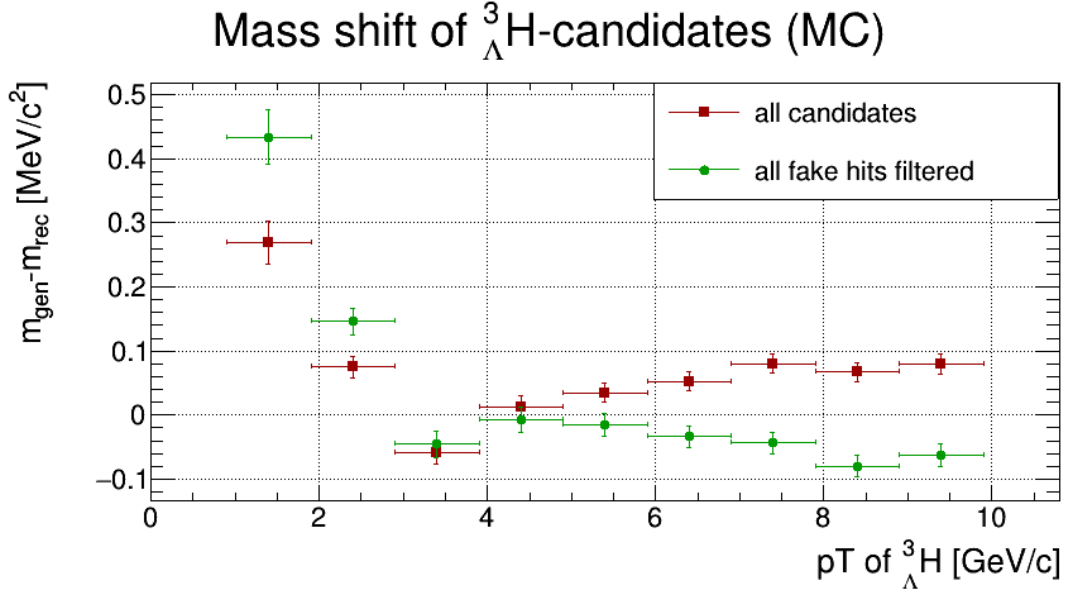


Figure 4.11: Comparison of mass shifts of MC simulated candidates in different p_T -intervals with fake hits rejected and not rejected. The values were obtained by Voigt fits.

Candidates with fake hits		
Track containing fake hit	Percentage	Percentage (excluding last crossed layer)
Pion	27.5%	13.2%
Proton	16.2%	5.0%
Deuteron	20.7%	6.2%
Any track	41.9%	20.1%

Table 4.1: Percentage of candidates with fake hits and for which daughter track the fake hits occur. The second column shows the averages from figure 4.10, the third shows the averages from figure 4.12.

The first approach is to somewhat redefine the meaning of a fake hit: as it was explained before, if a candidate decays shortly after an ITS layer, the daughter tracks are assigned the ITS cluster belonging to the candidate. The influence on the resulting daughter tracks should not be very big in this case, since they will not be artificially prolonged by a large margin. By requiring tracks to have no fake hits in the layers before the last layer the ${}^3_{\Lambda}H$ -candidate crossed, only tracks which have been artificially prolonged by at least the distance separating two subsequent ITS layers are rejected. The amount of rejected tracks is visualized in figure 4.12 and the average percentages are reported in table 4.1. Figure 4.13 shows the influence this has on the mass shift in different transverse momentum regions. Above $p_T > 4 \text{ GeV}/c$, the mass shift seems to be reduced compared to the average mass shift of all candidates, but also compared to the absolute value of the mass shift when rejecting fake hits in all layers, as reported in figure 4.11. Table 4.1 indicates that around 20% of candidates are rejected with this condition, so only roughly half of the candidates that were rejected before.

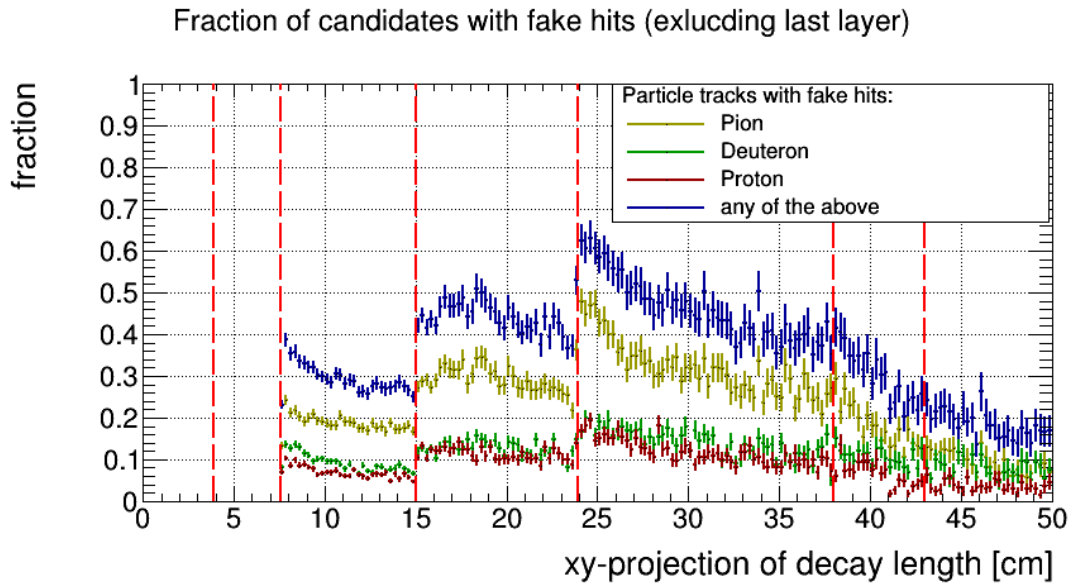


Figure 4.12: Share of candidates with fake hits, while excluding fake hits in the last layer each candidate has crossed. Positions of ITS layers again indicated by the red dashed lines.

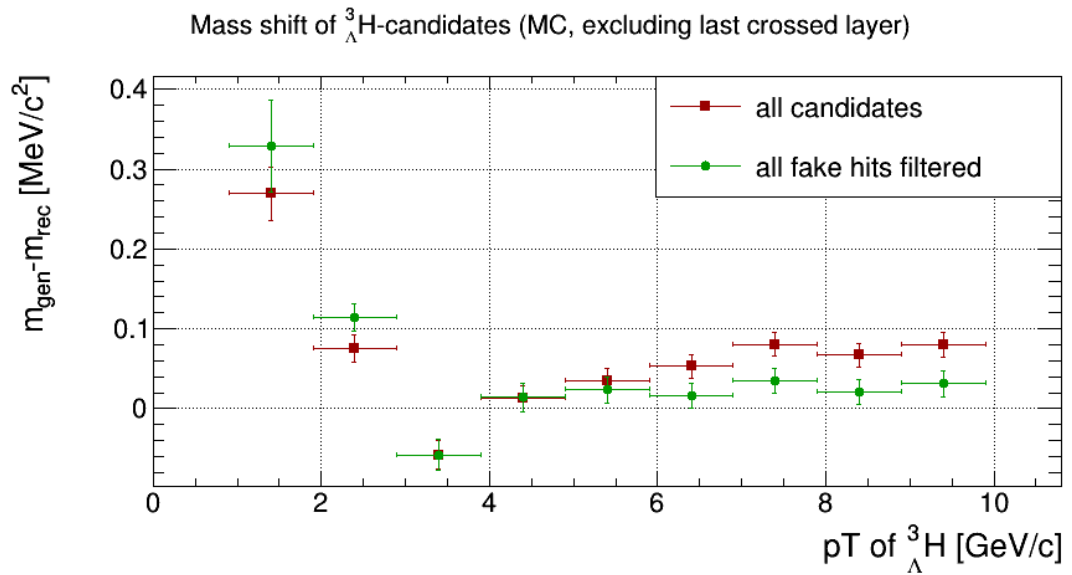


Figure 4.13: Comparison of mass shifts of MC simulated candidates in different p_T -bins with fake hits rejected and not rejected, while excluding fake hits in the last layer crossed by the candidate. The values were obtained by Voigt fits.

The second approach is to check which of the daughter tracks contain a fake hit and rejecting only fake hits from one of the daughters, while allowing fake hits for the other two. Again, table 4.1 shows how many candidates are rejected, if the rejection depends on the which daughter is assigned a fake hit. The investigation was repeated for each daughter and the lowest mass shift was obtained, when only rejecting candidates where the proton track had a fake hit, as is illustrated in figure 4.14. Here, only 16% of candidates are eliminated and the mass shift is close to zero for $p_T > 4 \text{ GeV}/c$. However, this approach still lacks physical reasoning and was tested solely for the sake of decreasing the amount of rejected candidates. Since the fake hits could effect the reconstructed momentum of the daughters, the effects on the mass measurement could vary, depending on which daughter track contains the fake hit, but this will have to be investigated in the future.

In conclusion, both these approaches decreased the amount of rejected candidates and the average mass shift of the reconstructed candidates was lowered to a fairly small value of around 0-25 keV at $p_T \geq 4 \text{ GeV}$. For future analyses of real data, it has to be studied if rejecting more than 15% of candidates is worth the benefits one gains from applying these selections. It would also be interesting to see, if and how much background is rejected by this, since this could also help in deciding if this criteria is reasonably applicable in upcoming measurements.

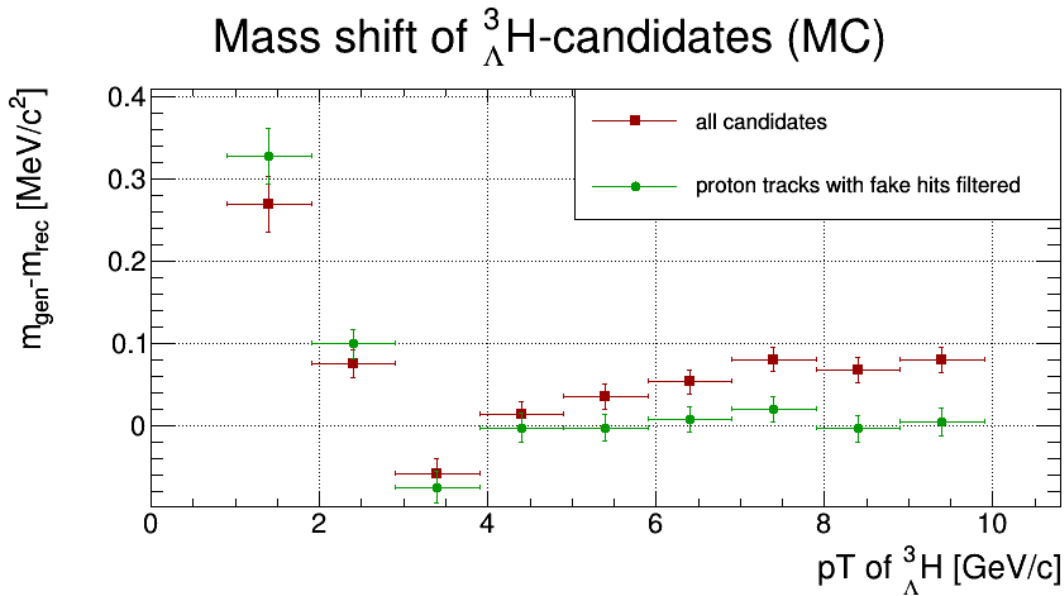


Figure 4.14: Comparison of mass shifts of MC simulated candidates in different p_T -bins with fake hits in the proton track rejected and not rejected.

4.5 Selection of ${}^3_{\Lambda}H$ -candidates

4.5.1 Event selection

The events that will be analyzed in the following sections are Pb-Pb collisions recorded in 2018 at a center-of-mass energy per nucleon pair of $\sqrt{s_{NN}} = 5.02$ TeV and with 0-90% centrality. Some standard selections for Pb-Pb events have been applied: the primary vertex is required to be within ± 10 cm of the nominal interaction point and *pile-up* events, where tracks from more than one primary collision have to be simultaneously processed by the detector, are also rejected. Additionally, the number of contributors to the primary vertex is required to be ≥ 2 .

The number of analyzed events is 10^8 central collision events (0-10% centrality), 10^8 peripheral collision events (30-50% centrality) and $0.5 \cdot 10^8$ events in both the centrality classes 10-30% and 50-90%.

4.5.2 Candidate selection

When trying to study 3-body decays from ${}^3_{\Lambda}H$ it is necessary to pose strict requirements on the reconstructed candidates to reduce the large combinatorial background. In this section, a first outline of a possible candidate selection will be given and its performance will be studied. The candidate selection used in [22] for measuring the lifetime of ${}^3_{\Lambda}H$ via the 3-body decay will be used as a starting point.

The previously mentioned selections for tracks in the MC simulation, summarized in tables 3.2 and 3.3, will also be applied to data. On top of that, the selections summarized in table 4.2 will be applied.

Candidate Selection	
Variable	Selection
Fake Hits (excluding last layer)	rejected for $p_T \geq 4$ GeV/c
$\cos(\alpha)$	≥ 0.9995
DCA_{π}^{PV}	≥ 0.2 cm
$\text{DCA}_{p,\pi}$	≤ 0.2 cm
$\text{DCA}_{d,\pi}$	≤ 0.2 cm
$\text{DCA}_{p,d}$	≤ 0.1 cm
$\text{DCA}_{daughters}^{SV}$	≤ 0.05 cm
Opening Angle $\beta_{p,\pi}$	≤ 0.5
Opening Angle $\beta_{d,\pi}$	≤ 0.4

Table 4.2: First iteration of a candidate selection that could be applied to real data for measuring the mass of ${}^3_{\Lambda}H$.

Here, the pion's DCA to the primary vertex is required to be larger than 0.2 cm, which rejects a large portion of primary pions⁵. The DCAs between two daughter tracks are also restricted, as well as the DCAs of the daughters to the secondary vertex. Both these criteria ensure the quality of the secondary vertex. They were adopted from [22] and they have been confirmed to be reasonable by checking their

⁵Primary pions are responsible for a significant fraction of the combinatorial background, which is why most cuts involving pions are stricter than cuts only involving the other daughters.

distributions in the MC dataset. This is also the case for the cuts on the opening angle β between two daughter tracks.

Tracks containing fake hits in layers before the last layer crossed by the candidate are also rejected for $p_T \geq 4 \text{ GeV}/c$, as was described in section 4.4.

The cut on $\cos(\alpha)$ is a lot stricter than before, which is due to the observed shape of this variable's distribution in the MC simulation, shown in figure 4.15. Note that the y axis has a logarithmic scale, so the distribution of MC candidates increases by two orders of magnitude when approaching $\cos(\alpha) = 1$ while the distribution in data is mostly flat.

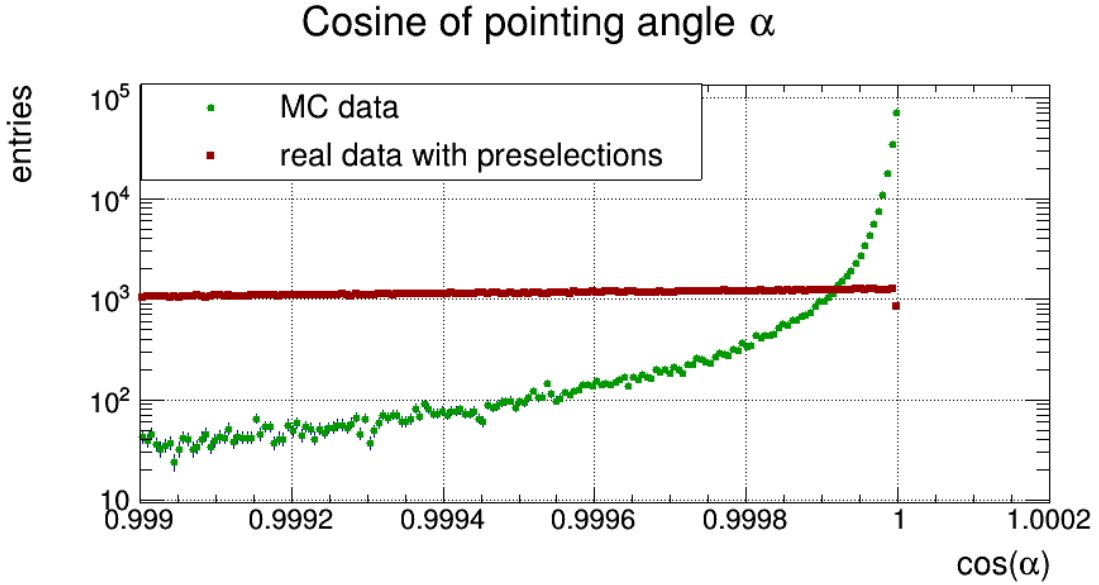


Figure 4.15: Distribution of the cosine of the pointing angle α for MC candidates and candidates in real data.

Efficiency of candidate selection

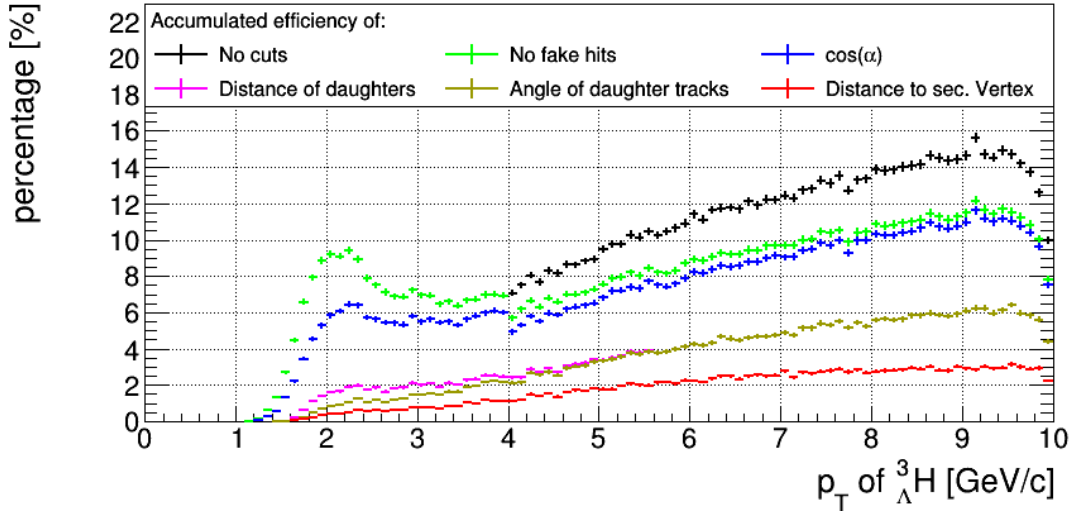


Figure 4.16: Remaining efficiency after subsequently applying the selection criteria in table 4.2. The criteria shown in the legend were applied from left to right and then from top to bottom. The efficiency was determined by comparing the number of ${}^3_{\Lambda}H$ -particles injected into the MC simulation with the number reconstructed candidates successfully passing each selection.

In figure 4.16 the efficiency of the candidate selection from table 4.2 is shown⁶. From this plot it can be seen which of the selection criteria cause the efficiency to decrease significantly: rejecting fake hits decreases the efficiency by about 20%. This was expected, as reported in table 4.1. The other two criteria causing a significant decrease are the cuts on the DCAs between two daughters and on the the DCAs of the daughters towards the secondary vertex, both of which reduce the efficiency by roughly 50%.

After this candidate selection, the remaining efficiency is 1%-3% across the whole p_T -spectrum. Currently, there is no published data from the ALICE collaboration on the 3-body decay of ${}^3_{\Lambda}H$, but since the systematic optimization of the candidate selection was not part of this work, it is expected that a significantly higher efficiency can be achieved, for example by utilizing machine learning techniques in the optimization process.

4.5.3 Signal in data collected by ALICE

Even though the efficiency is relatively low, the reported selection can still be used to extract a signal from the collected dataset, as is shown in figure 4.17. These plots clearly show the large portion of combinatorial background that was previously mentioned, since most of the entries in the histograms fall into that category. Only the entries between the line for the fit and the line for the background can be considered "true" candidates. The results of the Voigt-fits are summarized in table 4.3. The values for the mass show an increase at higher p_T with a difference from the largest to the lowest value of more than 3σ . The uncertainties u on the mass values

⁶The line labeled "Distance of daughters" includes the cut on DCA_{π}^{PV} , as well as the cuts on the DCAs between daughter tracks. "Angle of daughter tracks" includes cuts on the opening angles.

were calculated from the *Full Width Half Maximum* (FWHM) of the Voigt-function, for which an approximation is given by

$$F_{Voigt} \approx 0.5346 f_b \cdot \sqrt{0.2166(f_b)^2 + (f_g)^2}, \quad (4.7)$$

which is reported to have a maximal inaccuracy of 0.02% [19]. Here f_b and f_g are given by the FWHMs of the Breit-Wigner and Gaus-distributions:

$$f_b = 2\gamma \quad (4.8)$$

and

$$f_g = \sqrt{8 \ln 2} \sigma, \quad (4.9)$$

where γ and σ are defined as in equation 4.4. The uncertainty on the peak position of a Gaussian distribution is given by

$$u_{gaus} = \frac{\sigma}{\sqrt{N}}, \quad (4.10)$$

where N denotes the amount of entries in the distribution (which is equivalent to the integral over the distribution). To approximate the mass uncertainty of a Voigt-fit, the Voigt-function is treated as a Gaussian and a value for σ is extracted by setting equal the expressions for the FWHM of a Voigt-function (equation 4.7) and the FWHM of a Gaussian (equation 4.9), then solving for σ and implementing it in equation 4.10, resulting in:

$$u \approx \frac{F_{Voigt}}{\sqrt{8 \ln 2} \cdot N} \quad (4.11)$$

where N is calculated by integrating the fitted Voigt-function over the whole range after the background has been subtracted.

Since the separation energy of the Λ to the deuteron core was measured to be at 130 ± 50 keV [9], the current candidate selection does not produce a signal with which it would be possible to calculate a comparable result. The reason for this is that the uncertainties of the measured mass values exceed the value for separation energy. To be able to accurately measure this quantity a much higher efficiency is needed while still rejecting almost all of the combinatorial background.

Fit results in data		
p_T -range [GeV/c]	Mean of Voigt-Fit [MeV/c ²]	χ_{red}^2
2 - 3	2991.55 ± 0.22	0.39
3 - 4	2992.61 ± 0.26	0.56
4 - 5	2993.56 ± 0.29	2.49
5 - 7	2993.59 ± 0.39	1.41

Table 4.3: The results of the Voigt-fit for the distributions shown in figure 4.17.

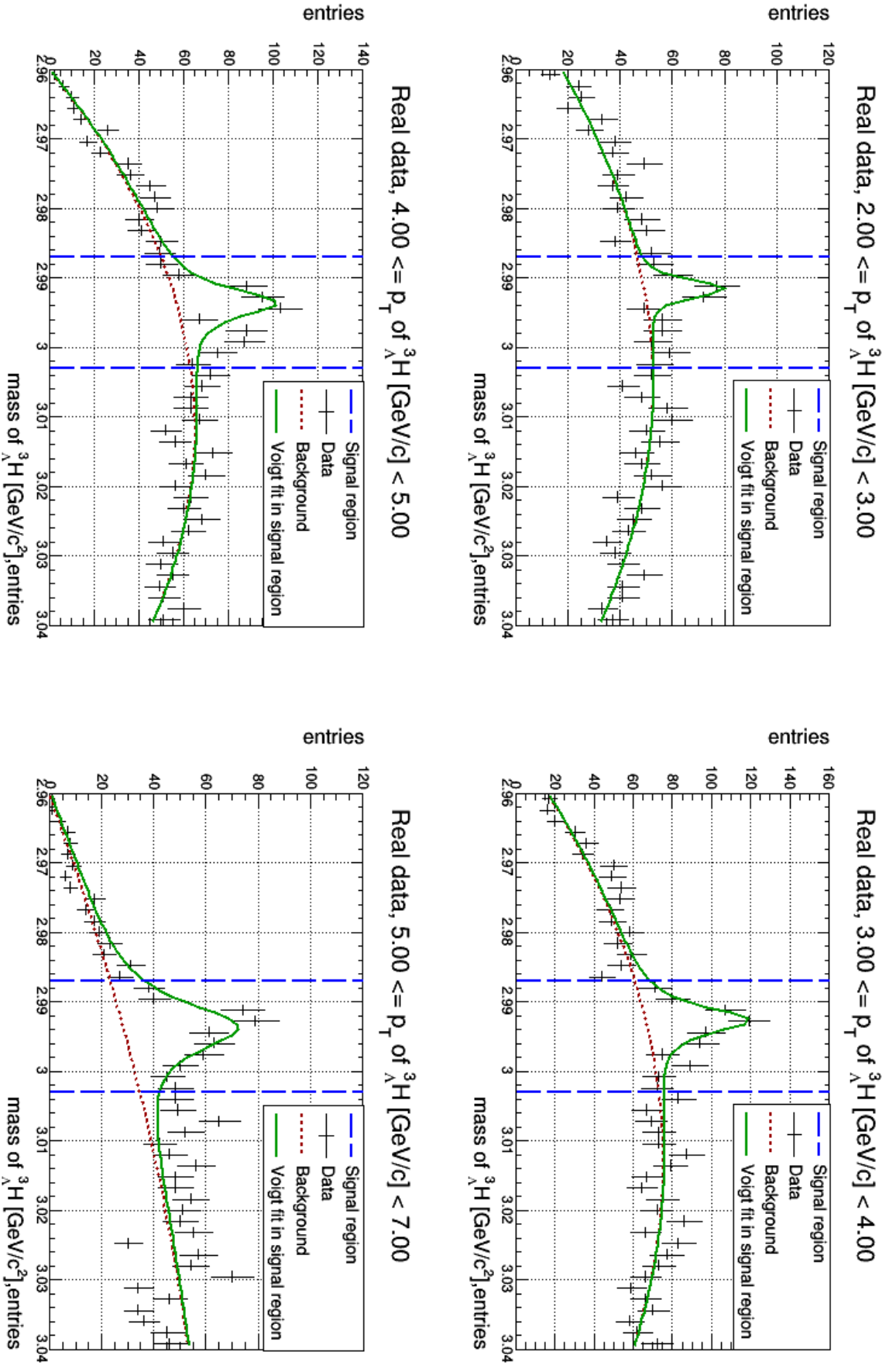


Figure 4.17: Signal of ${}^3\Lambda H$ in different p_T -regions. The background is described by a polynomial of second order and has been fitted outside the blue lines. The signal itself was fitted with a Voigt-function in the region between the blue lines. Specifics on the fit can be seen in table 4.3.

4.5.4 Mass resolution in Monte Carlo simulations

From equation 4.11 it is clear that reducing the uncertainties of the mass measurement means either increasing the resolution of the reconstruction and/or successfully reconstructing more "true" candidates. The resolution is heavily dependent on the detector collecting the data, but it can also be influenced by the candidate selection. To study this and to accurately compare the uncertainties on the mass in data to the ones in MC, simulated experiments similar to the ones in section 4.2 were conducted using a fixed amount of candidates from the MC dataset. This amount was obtained by combining the first three p_T -bins of figure 4.17 and integrating the obtained fit (excluding background), which results in a candidate count of 523. The returned mass value of the fit is $(2992.65 \pm 0.18) \text{ MeV}/c^2$. The distribution and the fit are shown in figure 4.18.

The simulated experiments were performed as follows: a distribution containing 523 simulated candidates (from the same p_T -range as in figure 4.18) has been fitted with a Voigt-function and the uncertainty on the mass has been calculated via equation 4.11. The results are shown in figure 4.19, which is a histogram showing how many of the experiments showed an uncertainty falling into the range of each bin. The experiments conducted with candidates which are required to pass the candidate selection from the previous sections show the lowest uncertainties (with around 60 keV), but with a candidate selection this strict the remaining candidates in the MC simulations only allow for 12 simulated experiments. Using all MC candidates in the p_T -range of 2 GeV/c to 5 GeV/c, 99 experiments can be performed and the uncertainties are systematically higher with an average of around 100 keV. This indicates that the candidate selection is more likely to reject candidates at the edges of the distribution, resulting in a sharper peak when comparing to a distribution without cuts, but with the same amount of entries.

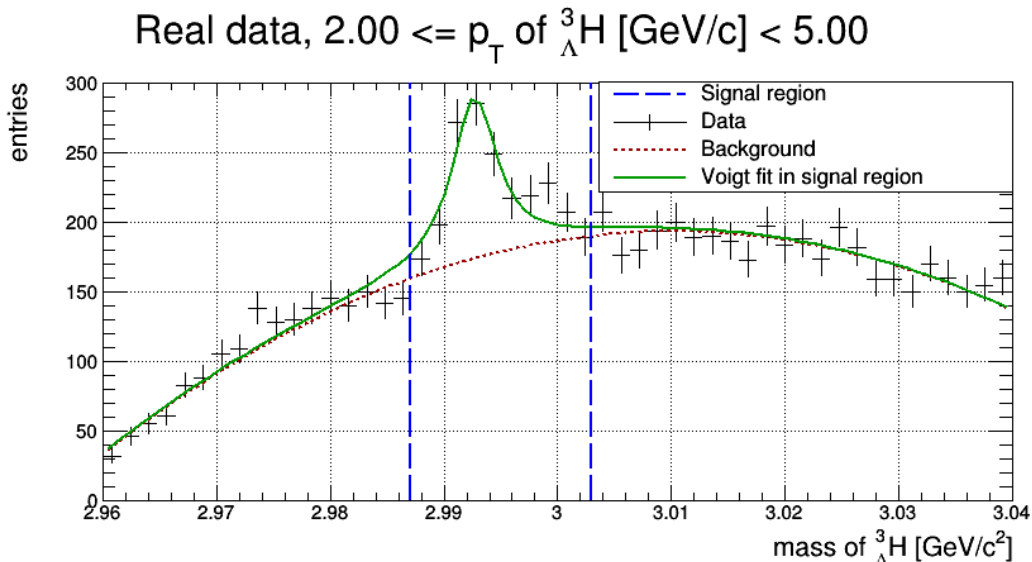


Figure 4.18: Signal of ${}^3_{\Lambda}H$ in the specified p_T -region. The fit was performed the same way as for figure 4.17.

The green points in figure 4.19 should be the most accurate simulation of the circumstances in figure 4.18, since all the candidates have passed the same candidate selection and both distributions contain the same amount of candidates when excluding background. However, the uncertainty in data exceeds the one obtained from the MC simulation by a factor of 3. The uncertainties that were calculated from MC without a strict selection of candidates also differ from the uncertainty in data by a factor of roughly 2, even though the resolution is not artificially enhanced by selecting preferably candidates near the maximum. This indicates that there are effects in data, which artificially broaden the distribution, for example the shift towards higher masses at high transverse momentum that is evident from table 4.3. The results of this section indicate that measuring the mass of ${}^3_{\Lambda}H$ accurately enough to calculate the separation energy of the Λ is currently not possible. The unexpected increase of mass values for higher p_T in data will have to be studied in the future and the efficiency of the candidate selection needs to be increased to lower the uncertainty of the measurement. Also, potential other effects causing a broadening of the peak-widths will have to be studied and understood.

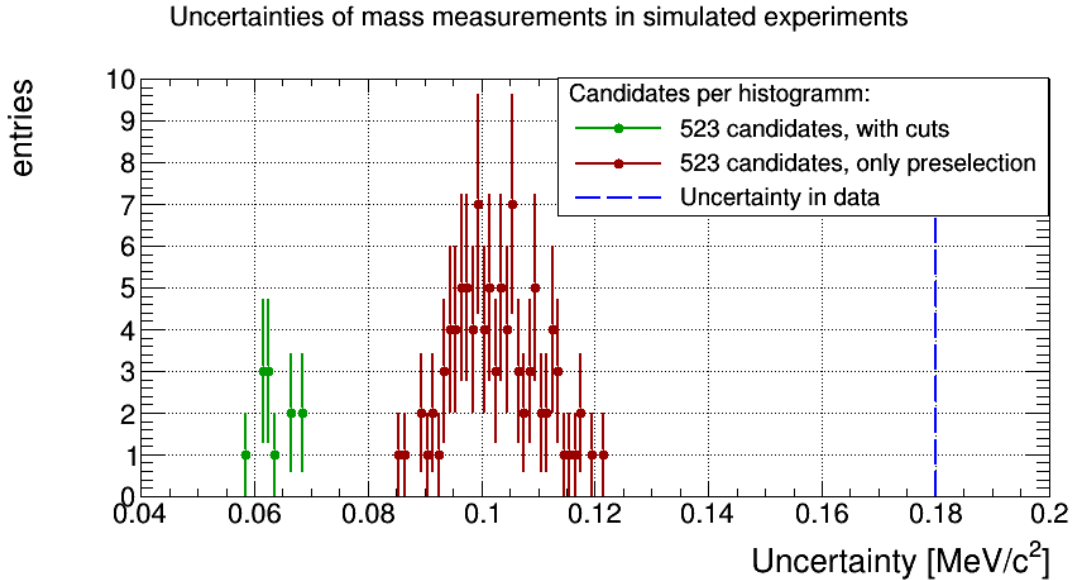


Figure 4.19: Histogram showing the number of experiments with a certain uncertainty. All candidates in the experiments are required to have a transverse momentum of $2 \text{ GeV}/c \leq p_T < 5 \text{ GeV}/c$. The green points show experiments conducted with 523 candidates that have passed the candidate selection used in data, the red ones show experiments conducted with 523 candidates that were not required to pass any additional selections, only the preselections for the MC simulation. The blue dashed line shows the uncertainty obtained from data in figure 4.18.

Chapter 5

Conclusion and Outlook

A MC sample of Pb-Pb collisions at $\sqrt{s_{NN}} = 5.02$ TeV in the ALICE detector was studied to determine a strategy for accurately measuring the mass of ${}^3_{\Lambda}H$ via the 3-body decay channel, using the KF particle package for candidate reconstruction. Different models for describing the recorded mass distributions were compared and the Voigt-function was determined to be the most accurate to describe the data.

Several investigations were made to decrease the difference between the mass values of reconstructed ${}^3_{\Lambda}H$ -candidates and the true ${}^3_{\Lambda}H$ -mass value in the simulations, which lead to a proposal for updating the mass values of several particle species in the KF package. Furthermore, the effects of using tracks with wrongly assigned ITS hits to reconstruct candidates were reviewed and possibilities of applying a candidate selection utilizing these wrongly assigned hits were explored.

The data recorded by ALICE in 2018 from Pb-Pb collisions at $\sqrt{s_{NN}} = 5.02$ TeV was analyzed by using a modified version of the candidate selection published in [22]. A signal was observed and is reported in this thesis. Discrepancies with respect to the expectations based on MC studies were found. They indicate the contribution from unexpected effects which will require further investigation.

A lot of studies covered in this thesis can be taken as a starting point for more in-depth investigations with the goal to accurately measure the mass of ${}^3_{\Lambda}H$: the effects from the detector and the reconstruction procedure causing the mass distributions to be described by a Voigt-function could be studied further, as well as the influences of tracks with "fake hits" on the mass measurement. The candidate selection for data should be further optimized in terms of efficiency and background rejection, which could be done with a machine learning approach, using the MC simulation as training data set.

The observed signal from the 2018 data will have to be systematically checked to understand the shift towards higher masses for higher p_T -regions and any potential contamination of the signal with wrongly identified/recombined candidates will have to be investigated and understood to enable an accurate determination of the mass and binding energy of ${}^3_{\Lambda}H$.

Acknowledgments

Working with the ALICE group in Heidelberg never failed to be an interesting and entertaining endeavor and I could always count on receiving a lot of support while learning to work scientifically, even during a year that posed novel challenges to all of us.

I want to thank my supervisors Sebastian Hornung and Alberto Caliva for providing continued guidance during my time in this group and I also want to thank Silvia Masciocchi for managing to find the time to supervise each of her many students individually, even during times, where it was not possible to meet anyone in person. Lastly, I want to thank my family and friends for the support I have received over the last years, since all of this would not have been possible without them.

List of acronyms

ALICE - A Large Hadron Collider Experiment
BR - Branching Ratio
CERN - Conseil Européen pour la Recherche Nucléaire
EMCal - Electro-Magnetic Calorimeter
FWHM - Full Width Half Maximum
ITS - Inner Tracking system
KF package - KFparticle vertexing package, (KF referring to *Kalman Filter*)
LHC - Large Hadron Collider
MC - Monte Carlo (referring to *Monte Carlo Simulation*)
PID - Particle Identification
PHOS - Photon Spectrometer
QCD - Quantum Chromo dynamics
QGP - Quark-Gluon Plasma
RMS - Root Mean Square
SM - Standard Model
TOF - Time Of Flight
TPC - Time Projection Chamber
TRD - Transition Radiation Chamber

Declaration of authorship

Ich versichere, dass ich diese Arbeit selbstständig verfasst und keine anderen als die angegebenen Quellen und Hilfsmittel benutzt habe.

Heidelberg, den 29. November 2020

Bibliography

- [1] E. Schnedermann et al. “Thermal phenomenology of hadrons from 200A GeV S+S collisions”. In: *Phys. Rev. C* 48, 2462 (1993).
- [2] S. Agostinelli et al. “GEANT4- a simulation toolkit”. In: *Nucl. Instrum. Meth. A* 506 (2003). DOI: 10.1016/S0168-9002(03)01368-8.
- [3] P. F. Bedaque and Ubirajara van Kolck. “Effective field theory for few-nucleon systems”. In: *Annu. Rev. Nucl. Part. Sci.* 2002, 52:339-96 (2002). DOI: 10.1146/annurev.nucl.52.050102.090637.
- [4] T. Boeckel and J. Schaffner-Bielich. “Little inflation at the cosmological QCD phase transition”. In: *Phys. Rev. D* 86, 103506 (2012).
- [5] Ignazio Bomaci. *The Hyperon Puzzle in Neutron Stars*. 2016. URL: <https://arxiv.org/abs/1601.05339v1>.
- [6] ALICE Collaboration. “ ${}^3_{\Lambda}H$ lifetime measurement in Pb–Pb collisions at $\sqrt{s_{NN}} = 5.02$ TeV via two body decay”. In: *Phys. Lett. B* 797, 134905 (2019). DOI: <https://doi.org/10.1016/j.physletb.2019.134905>.
- [7] ALICE Collaboration. “ ${}^3_{\Lambda}H$ production in Pb–Pb collisions at $\sqrt{s_{NN}} = 2.76$ TeV”. In: *Phys. Lett. B* 754, 360-372 (2016). DOI: <http://dx.doi.org/10.1016/j.physletb.2016.01.040>.
- [8] ALICE Collaboration. *Multiplicity dependence of light (anti-)nuclei production in p–Pb collisions at $\sqrt{s_{NN}} = 5.02$ TeV*. 2019. URL: <https://arxiv.org/pdf/1906.03136.pdf>.
- [9] D.H. Davis. “50 years of hypernuclear physics Part I., The early experiments”. In: *Nucl. Phys. A* 754, 3c-13c (2005). DOI: 10.1016/j.nuclphysa.2005.01.002.
- [10] M. Ivanov et al. “Track reconstruction in high density environment”. In: *Nucl. Instrum. Meth. A* 566, 70-74 (2006).
- [11] M. Tanabashi et al. “Review of Particle Physics”. In: *Phys. Rev. D* 98, 030001 (2018). DOI: 10.1103/PhysRevD.98.030001.
- [12] ALICE Collaboration et al. “Performance of the ALICE Experiment at the CERN LHC”. In: *arXiv:1402.4476 [nucl-ex]* (2014).
- [13] Esma Mobs et al. *LHC Accelerator Complex*. 2016. URL: <https://cds.cern.ch/record/2197559?ln=en>.
- [14] H. Kamada et al. “ π -mesonic decay of the hypertriton”. In: *Phys. Rev. C* 57, 4 (1997).
- [15] K. Aamodt et al. “The ALICE experiment at the CERN LHC”. In: *JINST* 3, S08002 (2008).

-
- [16] Sergey Gorbunov. “On-Line reconstruction algorithms for the CBM and ALICE experiments”. PhD thesis. Faculty of Computer Science and Mathematics of the Johann Wolfgang Goethe University in Frankfurt am Main, 2013.
- [17] Ulrich W. Heinz. *Concepts of Heavy-Ion-Physics (for the Latin-American School of High-Energy Physics)*. 2004. URL: <https://arxiv.org/abs/hep-ph/0407360>.
- [18] Lukas Layer. “Development of a fast simulation tool for vertexing studies in ALICE”. Physikalisches Institut of the University of Heidelberg, 2015.
- [19] J. J. Olivero and R. L. Longbothum. “Empirical Fits to the Voigt line width: a brief review”. In: *J. Quant. Spectrosc. Radiat. Transfer, Vol. 17, pp. 233-236* (1977).
- [20] Carolina Reetz. “Investigation of Charm Production and Validation of the KF Particle Package”. Physikalisches Institut of the University of Heidelberg, 2019.
- [21] Mark Thomson. *Modern Particle Physics*. 2013.
- [22] Stefano Trogolo. “Study of the production of (anti-)hypertriton at the LHC with the ALICE experiment”. PhD thesis. Università degli studi di Torino, Scuola di Dottorato in Scienze della Natura e della Tecnologie Innovative, Dipartimento di Fisica, 2018.
- [23] Xin-Nian Wang and Miklos Gyulassy. “HIJING: A Monte Carlo model for multiple jet production in pp, pA and AA collisions”. In: *Phys. Rev. D* **44**, 3501 (1991). DOI: 10.1103/PhysRevD.44.3501.